Neurobiology of Disease

Conserved and Distinct Functions of the Autism-Related Chromatin Remodeler CHD8 in Embryonic and Adult Forebrain Neurogenesis

Chen Dong,[1,2*] Chuntao Zhao,[1*] Xiang Chen,[1*] Kalen Berry,[1] Jiajia Wang,[1] Feng Zhang,[1] Yunfei Liao,[1] Rong Han,[1] Sean Ogurek,[1] Lingli Xu,[1] Li Zhang,[1] Yifeng Lin,[2] Wenhao Zhou,[2] Mei Xin,[1] Daniel A. Lim,[4] Kenneth Campbell,[3] Masato Nakafuku,[3] Ronald R. Waclaw,[1] and Q. Richard Lu[1]

[1]Department of Pediatrics, Division of Experimental Hematology and Cancer Biology, Cincinnati Children's Hospital Medical Center, Cincinnati, Ohio 45229, [2]Key Laboratory of Birth Defects, Children's Hospital of Fudan University, Shanghai 201102, China, [3]Division of Developmental Biology, Cincinnati Children's Hospital Medical Center, Cincinnati, Ohio 45229, and [4]Department of Neurological Surgery, University of California San Francisco, San Francisco, California 94143

The chromatin remodeler CHD8 represents a high-confidence risk factor in autism, a multistage progressive neurologic disorder, however the underlying stage-specific functions remain elusive. In this study, by analyzing *Chd8* conditional knock-out mice (male and female), we find that CHD8 controls cortical neural stem/progenitor cell (NSC) proliferation and survival in a stage-dependent manner. Strikingly, inducible genetic deletion reveals that CHD8 is required for the production and fitness of transit-amplifying intermediate progenitors (IPCs) essential for upper-layer neuron expansion in the embryonic cortex. p53 loss of function partially rescues apoptosis and neurogenesis defects in the *Chd8*-deficient brain. Further, transcriptomic and epigenomic profiling indicates that CHD8 regulates the chromatin accessibility landscape to activate neurogenesis-promoting factors including TBR2, a key regulator of IPC neurogenesis, while repressing DNA damage- and p53-induced apoptotic programs. In the adult brain, CHD8 depletion impairs forebrain neurogenesis by impeding IPC differentiation from NSCs in both subventricular and subgranular zones; however, unlike in embryos, it does not affect NSC proliferation and survival. Treatment with an antidepressant approved by the Federal Drug Administration (FDA), fluoxetine, partially restores adult hippocampal neurogenesis in *Chd8*-ablated mice. Together, our multistage functional studies identify temporally specific roles for CHD8 in developmental and adult neurogenesis, pointing to a potential strategy to enhance neurogenesis in the CHD8-deficient brain.

Key words: ATP-dependent chromatin remodeler; autism spectrum disorders; CHD8; embryonic and adult neurogenesis; neural stem/progenitors; transit-amplifying intermediate progenitor

Significance Statement

The role of the high-confidence autism gene *CHD8* in neurogenesis remains incompletely understood. Here, we identify a stage-specific function of CHD8 in development of NSCs in developing and adult brains by conserved, yet spatiotemporally distinct, mechanisms. In embryonic cortex, CHD8 is critical for the proliferation, survival, and differentiation of both NSC and IPCs during cortical neurogenesis. In adult brain, CHD8 is required for IPC generation but not the proliferation and survival of adult NSCs. Treatment with FDA-approved antidepressant fluoxetine partially rescues the adult neurogenesis defects in CHD8 mutants. Thus, our findings help resolve CHD8 functions throughout life during embryonic and adult neurogenesis and point to a potential avenue to promote neurogenesis in CHD8 deficiency.

Received Dec. 4, 2021; revised Aug. 18, 2022; accepted Aug. 23, 2022.

Author contributions: Q.-R.L. and C.D. designed research; C.D., C.Z., X.C., K.B., J.W., Y.L., R.H., and S.O. performed research; F.Z., L.X., L.Z., Y.L, W.Z, M.X, D.A.L, K.C, M.N., and R.R.W. analyzed data; C.D. wrote the paper.

This work was supported by Cincinnati Children's Research Foundation to Q.-R.L. K.B. was supported by National Institutes of Health–National Cancer Institute Grant 2T32CA117846-11A1. We thank Dr. Ryo Kageyama for the Nestin-CreERT2 mouse line and Drs. Paul Andreassen, Ed Hurlock, and Rachid Drissi for comments and technical help. C.D. performed the experiments at the Cincinnati Children's Hospital and current affiliation is the Children's Hospital of Fudan University.

C. Dong's present address: Children's Hospital of Fudan university, Shanghai 201102, China.

*C.D., C.Z., and X.C. contributed equally to this work.

The authors declare no competing financial interests.

Correspondence should be addressed to Q. Richard Lu at richard.lu@cchmc.org.

https://doi.org/10.1523/JNEUROSCI.2400-21.2022

Introduction

Autism spectrum disorder (ASD) is a multistage progressive disorder with significant genotypic and phenotypic complexity (An and Claudianos, 2016; Courchesne et al., 2019). Deficits in early neural development are commonly believe to underly autism etiology (Packer, 2016; Varghese et al., 2017). However, the clinical symptoms of ASD persist into adulthood (Bernier et al., 2014; Courchesne et al., 2019); currently, the mechanisms that link autism-risk factors to stage-specific defects during developmental and adult neurogenesis remain incompletely understood.

Neurogenesis is essential for the production of the proper number of neurons and glial cells from neural stem cells (NSCs) and neural progenitor cells (NPCs) in the brain and occurs throughout life (Hsieh and Gage, 2004; Delgado et al., 2020). In the developing cortex, stem-like radial glial cells (RGCs) differentiate into neurons either directly from NPCs or indirectly via secondary basal progenitors such as intermediate progenitor cells (IPCs) marked by TBR2 [also known as EOMES (Eomesodermin); Noctor et al., 2004; Kriegstein and Alvarez-Buylla, 2009; Mihalas et al., 2016]. In contrast to direct neurogenesis, which only produces limited neurons per cell cycle, indirect neurogenesis enables phenomenal production and amplification of cortical neurons, particularly those destined to form the superficial layers, and leading to expansion of the mammalian cortex during evolution (Cardenas et al., 2018; Borrell, 2019). Transit-amplifying IPCs are vital for generating appropriate numbers of upper-layer excitatory neurons (Sessa et al., 2008; Kriegstein and Alvarez-Buylla, 2009), a process known to be disrupted in autism (Velmeshev et al., 2019).

In the adult brain, neurogenesis occurs in two specific regions, the subventricular zone (SVZ) and subgranular zone (SGZ). Newborn neurons differentiated from a population of IPCs in the SVZ migrate via the rostral migratory stream to the olfactory bulb and differentiate further into interneurons, whereas new dentate granule cells are generated from the SGZ neural progenitor cells in the hippocampus (Ming and Song, 2011; Hsieh and Zhao, 2016; Obernier et al., 2018). Adult neurogenesis has been shown to be critical for normal neuronal functions and neural circuitry (Aimone et al., 2006; Deng et al., 2010; Song et al., 2012).

Previous studies showed that loss-of-function disruptive mutations in *CHD8*, encoding the ATP-dependent-chromodomain-helicase-DNA-binding-protein-8, can cause ASD (Bernier et al., 2014; Cotney et al., 2015; Stolerman et al., 2016). Haploinsufficient mutation or knockdown animal models share several clinical features with ASD patients including impaired cortical development and plasticity, macrocephaly, social behavioral abnormalities, and intellectual impairment (Durak et al., 2016; Katayama et al., 2016; Gompers et al., 2017; Platt et al., 2017; Jung et al., 2018; Suetterlin et al., 2018; Xu et al., 2018; Jiménez et al., 2020; Ellingford et al., 2021; Hurley et al., 2021). Gene knockout studies indicate that *Chd8* is critical for cortical progenitor development and survival as well as neural specification from embryonic stem cells (ESCs; Sood et al., 2020; Hurley et al., 2021; Kweon et al., 2021). However, at present, the stage- and cell-type-specific effects of the CHD8 loss of function on neural progenitor survival and neurogenic processes in developing and adult brains remain elusive.

In this study, we use developmentally regulated and neural progenitor-specific *Chd8* ablation approaches to investigate the effect of CHD8 on embryonic and adult neurogenesis and find that CHD8 ablation in NSCs impairs their proliferation and survival in a stage-dependent manner. Strikingly, we identify a critical requirement for CHD8 in the generation and survival of transit-amplifying IPCs for indirect neurogenesis. Transcriptomics and epigenomic analyses further indicate that CHD8 maintains proper chromatin landscape and regulates neurogenesis-related programs including TBR2, a key regulator of IPC neurogenesis. In the adult brain, CHD8 ablation in NSCs inhibits neurogenesis via IPCs in both forebrain SVZ and hippocampal SGZ; however, it does not affect NSC proliferation and survival. Furthermore, pharmacological enhancement of NSC differentiation by the antidepressant fluoxetine, approved by the Federal Drug Administration (FDA), partially enhances neurogenesis in CHD8-depleted adult mice. Thus, our observations reveal that CHD8 exhibits conserved, yet spatiotemporally distinct, functions in developmental and adult neurogenesis, pointing to a potential therapeutic avenue of augmenting neurogenesis in the CHD8-deficient brain.

Materials and Methods

Animals

Mice homozygous for *Chd8* floxed alleles ($Chd8^{fl/fl}$; Zhao et al., 2018) were crossed with $Emx1\text{-}Cre^{+/-}$ mice (Gorski et al., 2002; from Kenneth Campbell) to generate *Chd8* conditional KO (cKO; $Chd8^{fl/fl}$;$Emx1\text{-}cre^{+/-}$), *Chd8* cHet ($Chd8^{fl/+}$;$Emx1\text{-}cre^{+/-}$), and their littermate wild-type control. Nestin-CreER$^{+/-}$ mice (from Ryo Kageyama) were crossed with *Chd8*-flox mice to generate *Chd8* inducible KO (iKO; $nestin\text{-}Cre^{ERT2+/-}$; $Chd8^{fl/fl}$) and its control ($nestin\text{-}Cre^{ERT2+/-}$). Nestin-Cre mice (stock #003771) and the reporter mice CAG-CAT-EGFP (ccGFP; stock #024636) were obtained from The Jackson Laboratory. We bred the ccGFP reporter line with $Chd8^{fl/fl}$ mice to obtain $Chd8^{fl/+}$; $ccGFP^{+/-}$ mice, which then crossed with *Chd8* cHet mice to produce *Chd8* cKO, ccGFP ($Chd8^{fl/fl}$;$Emx1\text{-}cre^{+/-}$;$ccGFP^{+/-}$) and *Chd8* cHet, ccGFP ($Chd8^{fl/+}$;$Emx1\text{-}cre^{+/-}$; $ccGFP^{+/-}$) mice for fluorescence-activated cell sorting (FACS) and assay for transposase-accessible chromatin using sequencing (ATAC-seq) in relation to wild-type or $Chd8^{fl/fl}$ controls. Both male and female animals were used in the developmental and behaviors study. All mice used in experiments were maintained on a mixed C57/Bl6;129Sv background and housed in a pathogen-free vivarium with a 12 h light/dark cycle and normal chow food and water *ad libitum*. Mouse embryos harvested at different ages with embryonic day (E)0.5 considered the time of vaginal plug. All animal experiments were approved by the Institutional Animal Care and Use Committee of Cincinnati Children's Hospital Medical Center.

Tamoxifen and fluoxetine administration

Tamoxifen (TAM; catalog #T5648, Sigma-Aldrich) was dissolved in a vehicle of ethanol and sunflower seed oil (1:9 v/v; catalog #S5007, Sigma-Aldrich) as a concentration of 20 mg/ml. For adult neurogenesis experiments, mice were intraperitoneally injected with 100 µl tamoxifen once daily for 5 consecutive days. For embryonic-stage-specific experiments, pregnant mice on certain embryonic days were intraperitoneally injected with tamoxifen (100 mg/kg) once daily for 3 consecutive days. Fluoxetine (FLX) was obtained from Spectrum Chemical. Mice in adult neurogenesis rescue experiments were intraperitoneally injected with FLX 15 mg/kg daily for 21 d (Ohira et al., 2013). Treatments were administrated to both control and mutant mice. Mice were analyzed at different days after tamoxifen administration as designed.

Tissue processing, immunohistochemistry, and immunoblotting

Mice at defined ages were anesthetized with isoflurane and transcardially perfused with PBS, pH 7.4, followed by 4% PFA. Embryonic and postnatal brains were dissected and fixed in 4% PFA for 45 min (embryonic) and 2 h (postnatal) at 4°C. After washing in PBS, brain samples were dehydrated in 25% sucrose over night at 4°C, embedded in optimal cutting temperature medium, and cryosectioned at 20 µm. For those paraffin sectioned samples, dissected brains were fixed in 4% PFA overnight,

embedded in paraffin, and sectioned at 5 μm. Both male and female animals were used for the study.

Cryosection slides were washed in PBS three times followed by permeabilization with 0.2% Triton X-100 in PBS for 20 min and blocking with blocking buffer (5% normal donkey serum in PBS) at room temperature. Primary antibodies were incubated overnight at 4°C. Antibodies used in the study were the following: rabbit anti-CHD8 (catalog #ab84527, Abcam), rabbit anti-Cux1 (catalog #sc-13024, Santa Cruz Biotechnology), rat anti-CTIP2 (catalog #ab18465, Abcam), mouse anti-TUJ1 (catalog #801201, BioLegend), goat anti-Sox2 (catalog #sc-17320, Santa Cruz Biotechnology), mouse anti-p53 (catalog #2524, Cell Signaling Technology), rabbit anti-cleaved caspase 3 (catalog #9661, Cell Signaling Technology), rabbit anti-TBR2 (catalog #ab23345, Abcam), rabbit anti-phospho-Histone H3, pH 3 (catalog #PA5-17869, Thermo Fisher Scientific), mouse anti-BrdU (5-Bromo-2′-deoxyuridine; catalog #555627, BD Pharmingen), rat anti-BrdU (catalog #ab6326, Abcam), mouse anti-neuronal nuclei (NeuN; catalog #MAB377, Millipore), goat anti-doublecortin (DCX; catalog #sc-8066, Santa Cruz Biotechnology), rabbit anti-PAX6 (catalog #ab5790, Abcam), rabbit anti-GFAP (catalog #13-0300, Cell Signaling Technology), rabbit anti-Iba1 (catalog #019-19741, Wako Pure,), mouse anti-γH2A.X (catalog #05-636, Millipore), rabbit anti-Calbindin (CB; catalog #13176, Cell Signaling Technology), rabbit anti-Tyrosine Hydroxylase (TH; catalog #13106, Cell Signaling Technology), mouse anti-Nestin (catalog #ab6142, Abcam), rabbit anti-OLIG2 (catalog #AB9610, Millipore), and rat anti-PDGFRα (catalog #558774, BD Biosciences). After washing in PBS, sections were incubated with secondary antibodies conjugated to Cy2, Cy3, or Cy5 (1:500; Jackson ImmunoResearch) and DAPI at room temperature for 2 h, washed in PBS, and mounted with Fluoromount-G (SouthernBiotech). For BrdU immunostaining, after normal staining for other required antibodies, sections were subjected to DNA denaturation with 2N hydrochloric acid at 37°C for 40 min, then neutralized with 0.1 M sodium borate, pH 8.5, for 2 × 8 min and normal immunostaining protocol with anti-BrdU antibody. For Nissl staining, paraffin section slides were deparaffinized, rehydrated, and subjected to cresyl violet. All immunofluorescence-labeled images were acquired using a Nikon $C2^+$ confocal microscope. Nissl staining images were acquired by Olympus BX53 Bright Field microscope.

The brains were sectioned at 20 μm by taking 1 μm serial optical thin sections for the quantification of labeled cells. Somata were defined as the counting unit. Every six sections were spaced 120 μm apart throughout the entire ventricular zone (VZ) and SVZ, and the hippocampus extent was used to assess the number of labeled cells and avoid any potential of double counting or tissue processing artifact on consecutive sections and ensure that the area counted for each brain is constant. A sequence of at least eight sections per animal (at least three animals per group) were obtained for 3D reconstruction with Imaris image software (Bitplane) to estimate the number of stained cells representing the entire volume of the brain tissue. Counts were also normalized to the length of VZ, SGZ, or cortical strip from the dorsolateral cortex as indicated in the figures. The cell counts were quantified by personnel blinded to the experimental condition of each sample. The quantification method is similar to those generally used for neurogenesis analysis (Feng et al., 2013; Insolera et al., 2014).

Behavior tests

For all behavior tests, mice we used were group housed (three or four animals per cage) in a temperature-controlled room with a 12 h light/dark cycle. Both male and female mice, 8 weeks old, were weaned in mixed genotype home cages, and experimenters blinded to genotype during testing and analysis were used according to a previous study (Durak et al., 2016). No previous analyses were performed on animals used for behavioral testing. All tests were conducted during the light cycle. Each apparatus was cleaned with dilute sodium hypochlorite solution before testing of each animal to prevent bias because of olfactory cues. Open field test was performed first as it is less stressful followed by the three chamber tests.

Open field test. Spontaneous exploratory and anxiety behavior was assessed following previously described procedures (Gould et al., 2009). Each animal was placed in the corner of an open-field apparatus (40 × 40 × 60 cm; Shanghai-Jiliang Software Technology), Total distance traveled and time spent outside of the central area (25% of total area) were automatically recorded over 15 min. The testing room was illuminated at 100 lux.

Three-chamber test. The three-chamber tests were performed in a black acrylic box with three chambers (20 × 30 cm). All mice were isolated for 3 d before the test. On the test day, the subject mice were first habituated in the center chamber for 10 min. In the sociability test, a novel (C57/BL strain) mouse (same sex as the subject mouse) was placed in a small metal container located in the center of the left-side chamber, and the object was placed in the other side. The wall between the compartments was removed to allow free access for the subject mouse to explore each of the three chambers. The duration of the time the subject mouse spent in each compartment was monitored. In the social novelty test, the first mouse (novel mouse) remained in one side of the chamber and now became a familiar social stimulus. The subject was tested in all three chambers (60 × 30 cm) for 10 min for each experiment. Time in each chamber was recorded automatically by EthoVision XT 14 software.

5-Iodo-2′-deoxyuridine/BrdU pulse labeling

Pregnant mice were sequentially injected with 100 mg/kg body weight with 5-Iodo-2′-deoxyuridine (IdU; catalog #I7125, Sigma-Aldrich) and BrdU (catalog #B9285, Sigma-Aldrich) intraperitoneally 2 h and 0.5 h, respectively, before being killed. Immunostaining was performed as described above with the BrdU antibody mouse anti-BrdU (catalog #555627, BD Pharmingen) which can recognize both IdU and BrdU, whereas the rat anti-BrdU antibody (catalog #Ab6326, Abcam) only recognizes BrdU.

Neural progenitor cell isolation and culture

Cortices of (E)14.5 control or *Chd8* cKO mouse embryos were dissected in cold PBS. Each culture was derived from an independent embryo. Cells were dissociated with Collagenase IV, followed with FACS sorting for reporter GFP^+ cells. All sorted cells grew in NPC maintenance medium composed of DMEM/F-12 (catalog #11320-033, Thermo Fisher Scientific), Neurobasal-A (catalog #10888-022, Thermo Fisher Scientific), B27 (catalog #12587-010, Thermo Fisher Scientific), 20 ng/ml FGF2, and 20 ng/ml EGF at 37°C, 5% CO_2. After 3 d, neurospheres were dissociated with StemPro Accutase (catalog #A11105-01, Thermo Fisher Scientific) into single-cell suspensions and plated at 50,000 cells/ml in NPC maintenance medium for neurosphere cultures. The primary sorted cells are considered first passage NPCs.

Assay for ATAC-Seq and analysis

ATAC-seq assays were performed as previously described (Buenrostro et al., 2015). We isolated ~50,000 GFP^+ cells using FACS from the cortices of E14.5 embryos, *Chd8* cKO, cHet, and control animals carrying a ccGFP reporter. Cells were lysed in cold lysis buffer, and their nuclei were isolated by spinning down at 500 × *g* for 10 min at 4°C. Immediately after the nuclei preparation, we performed the transposase reaction for 30 min at 37°C. Using a Qiagen MinElute kit, we purified DNA from cells. After DNA purification, libraries were generated using the Ad1_noMX and Ad2.1–2.4 barcoded primers and were amplified for 11 total cycles by NEBNext PCR master mix. The libraries were purified using a Qiagen MinElute kit to remove contaminating primer dimers. All libraries were then run on the Illumina Sequencer HiSeq 4000.

CHD8 chromatin immunoprecipitation followed by sequencing (ChIP-seq) data were downloaded from the previous study on the DRA database (Katayama et al., 2016). ATAC-seq data together with the downloaded ChIP-seq data files were then mapped to the mm10 genome assembly. Peak calling was performed by Model-Based Analysis of ChIP-seq (MACS; version 1.4.2, http://liulab.dfci.harvard.edu/MACS) with default parameters to get primary binding regions. To ensure that the data were of high quality and reproducibility, we called peaks with enrichment ≥10-fold over control ($p \leq 10^{-9}$) and compared the peak sets using the Encyclopedia of DNA Elements (ENCODE) overlap rules.

The identified primary regions were further filtered using the following criteria, to define a more stringent protein-DNA interactome: (1) The p value cutoff was set to $\leq 10^{-9}$, and (2) we required an enrichment of six-fold and peak height >5. Two samples of ATAC-seq or ChIP-seq data were combined by normalizing with reads number to generate heat maps. ChIP-seq data of histone marks were obtained from ENCODE database from mouse E14.5 whole brain (H3K4me3, https://www.encodeproject.org/experiments/ENCSR172XOZ/; H3K27ac and H3K27me3, https://www.encodeproject.org/experiments/ENCSR831YAX/). The heat maps of ChIP-seq data were drawn by the heat map tool provided by Cistrome (http://cistrome.org/ap). Visualized peaks figures were obtained from MochiView software, version 1.46, using WIG files generated by MACS or IGV (Integrative Genomics Viewer) software, version 2.3.51, using BIGWIG files. The heat map of ATAC-seq data were drawn by the plotHeatmap tool (https://deeptools.readthedocs.io/en/develop/content/tools/plotHeatmap.html). ToppGene (https://toppgene.cchmc.org/) were used to perform Gene Ontology (GO) analysis and pathway enrichment.

RNA sequencing and data analysis

RNAs from FACS-sorted GFP$^+$ cells of embryonic cortices were extracted by TRIzol (Life Technologies) following the standard protocol, then purified using RNeasy Mini Kit (Qiagen). The RNA quality was determined by Bioanalyzer (Agilent). NEBNext Poly(A) mRNA Magnetic Isolation Module (New England BioLabs) was used with a total of 1 µg of good-quality total RNA to isolate the poly A RNA as input. Libraries were prepared with the NEBNext Ultra II Directional RNA Library Prep Kit (New England BioLabs), which were dUTP-based stranded libraries. The library was indexed and amplified under a PCR cycle number of 8. After library Bioanalyzer QC analysis and quantification, individually indexed and compatible libraries were proportionally pooled and sequenced using NovaSeq 6000 Sequencing System (Illumina). Under the sequencing setting of single read 1 × 50 bp, ~25 million pass filter reads per sample were generated.

All RNA-Seq data were aligned to mm10 using TopHat with default settings (http://tophat.cbcb.umd.edu/). We used the cuffdiff command to estimate fragments per kilobase of transcript per million mapped reads values for known transcripts and to analyze differentially expressed transcripts. In all differential expression tests, a difference was considered significant if the FDR value was <0.1 ($p < 0.01$). Both raw and adjusted p values were used for the RNA-seq analysis. For the volcano plot, the upregulated and downregulated genes were represented by red or blue dots, respectively (fold change > 1.5, FDR < 0.1, $p <$ 0.01 between control and *Chd8* cKO). R language (http://www.r-project.org) was used for heat map drawing of gene expression. GO analysis and pathway enrichment were generated by ToppGene (https://toppgene.cchmc.org/).

For quantitative Real Time-PCR (qRT-PCR), cDNA was synthesized from 0.5 µg RNA by iScript Reverse Transcription Supermix (Bio-Rad) according to the instructions from the manufacturer. qRT-PCR was performed using the StepOnePlus Real-time PCR System (Applied Biosystems) with quantitative SYBR green PCR mix (catalog #170-8880, Bio-Rad).

Statistical analysis

Statistical data analyses were done using GraphPad Prism 7.0a software (https://www.graphpad.com). All data are shown as mean ± SEM. Data distribution was assumed to be normal, but this was not formally tested. Count data were assumed to be nonparametric, and appropriate statistical tests were used. Statistical significance was determined using two-tailed unpaired Student's t test and one-way or two-way ANOVA as indicated. Significance was set as $^*p < 0.05$, $^{**}p < 0.01$, and $^{***}p <$ 0.001, unless otherwise indicated. Quantifications were performed from at least three independent experiments or animals as indicated. No randomization was used to collect all the data, but they were quantified blindly.

Data availability

All the high-throughput sequencing data from RNA-seq and ATAC-seq generated in this study are deposited in the National Center for Biotechnology Information Gene Expression Omnibus under accession number GSE148608.

Results

Chd8 ablation in cortical NPCs leads to cortical malformations

To examine the expression pattern of CHD8 in the developing cortex, we performed immunostaining and showed that CHD8 was expressed in PAX6$^+$ RGCs/NPCs localized in the VZ and TBR2$^+$ IPC populations in the SVZ of the developing cortex at E14.5, as well as DCX$^+$ neural progenitors and NeuN$^+$ neurons in the postnatal cortex (Fig. 1*A*,*B*).

To determine whether CHD8 functions in cortical neurogenesis, we generated *Chd8* conditional knock-out (cKO) mice by crossing our *Chd8*$^{fl/fl\text{-Exon-4}}$ strain carrying exon-4 floxed alleles (Zhao et al., 2018) with an *Emx1-cre* line (Fig. 1*C*), which drives deletion mainly in cortical progenitors and their progeny starting from E9.5 (Gorski et al., 2002). In *Chd8*$^{fl/fl}$;*Emx1-cre*$^{+/-}$ mice (referred to here as *Chd8* cKO), CHD8 expression was depleted in cortical neurons compared with *Chd8*$^{fl/fl}$ mice (referred to as control mice; Fig. 1*D*). These *Chd8* cKO animals were born in expected Mendelian ratios and were viable throughout adulthood. Although the gross appearance and weight of mice appeared comparable to those of control mice, anatomic examination revealed severe forebrain malformations (Fig. 1*E*–*H*). Reduced cortical thickness was detected at both perinatal and adult stages in *Chd8* cKO mice (Fig. 1*G*,*H*). The phenotype of neocortical development in *Chd8* cKO mice is similar to that of another *Chd8* mutant mice (*Emx1-Cre;Chd8*$^{fl/fl\text{-Exon-3}}$) carrying *Chd8* exon-3 floxed alleles (Kweon et al., 2021). As *Emx1-Cre* predominantly targets dorsal cortical progenitors (Gorski et al., 2002), cerebellar and ventral brain regions are not grossly altered in the *Chd8* cKO relative to controls (Fig. 1*I*).

CHD8-deficient mice develop abnormal behaviors

Behavioral abnormalities, such as social deficits and other neuropsychiatric conditions like anxiety, are hallmarks of ASD (Simonoff et al., 2008; Lord et al., 2018; Takumi et al., 2020). To examine the potential abnormalities in social interaction and anxiety-related behaviors directly or indirectly caused by CHD8 deficiency, we performed two behavioral tests, an open field test) and a three-chamber test in control, heterozygous *Chd8* cHet (*Chd8*$^{fl/+}$;*Emx1-cre*$^{+/-}$), and *Chd8* cKO mice. Previous studies examining ASD-associated phenotypes in *Chd8* mutant mice had used both of these tests to assess anxiety-related behaviors and sociability deficits (Katayama et al., 2016; Jung et al., 2018; Suetterlin et al., 2018; Hurley et al., 2021; Kweon et al., 2021). We first subjected the mice to an open field test, which is widely used to measure anxiety-like behaviors in rodents (Gould et al., 2009; Seibenhener and Wooten, 2015; Kraeuter et al., 2019). *Chd8* cKO mice spent significantly less time in the center zone of the open field than control and *Chd8* cHet mice while reciprocally spending a longer time in the outer zones (Fig. 2*A*–*C*). The movement velocity was also higher in *Chd8* cKO mice than control and *Chd8* cHet mice (Fig. 2*D*), indicating hyperactivity in *Chd8* cKO mice. Notably, compared with control mice, *Chd8* cHet mice exhibited a phenotype similar to *Chd8* cKO mice, although to a lesser extent (Fig. 2*A*–*C*). These observations suggest that mice with CHD8 loss or dosage reduction in cortical NSCs develop anxiety-like behaviors and hyperactivity.

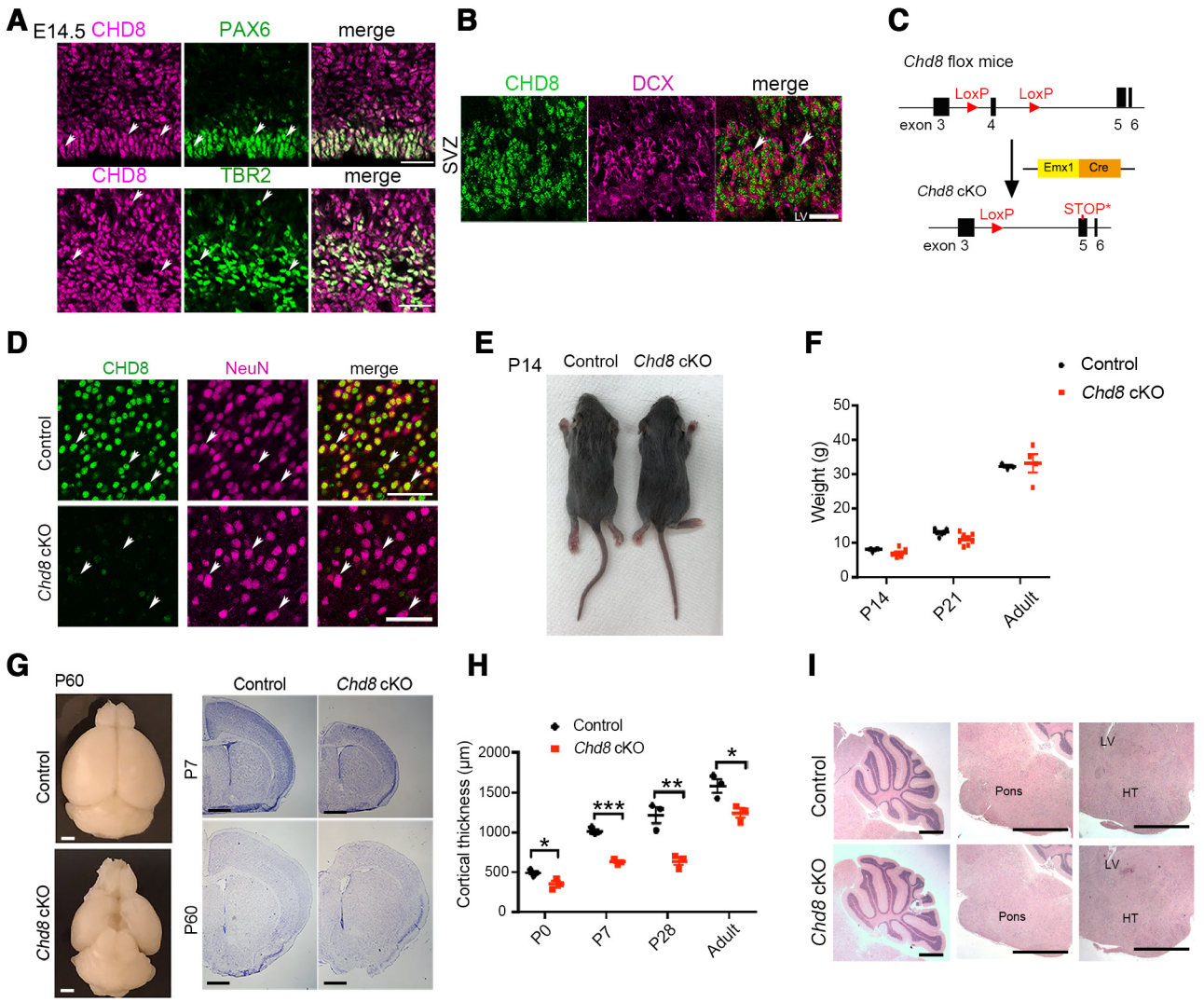

Figure 1. CHD8 expression is critical for cortical development. ***A***, Coronal section of cortical regions of E14.5 wild-type brain immunostained for CHD8 and PAX6 or TBR2. Arrows, co-labeled cells. Scale bars: 50 μm. ***B***, The SVZ region of wild-type brain was immunostained for CHD8 and DCX at postnatal day (P)7. Arrows, co-labeled cells. Scale bars: 20 μm. LV, lateral ventricle. ***C***, Schematic diagram of mating to knock out the region of *Chd8* in NPCs using the Emx1-Cre driver. ***D***, Control wild-type and *Chd8* cKO cortices were stained for CHD8 and NeuN at P21. Arrows indicated neurons. Scale bars: 20 μm. ***E***, Representative photographs of P14 control and *Chd8* cKO mice. ***F***, Quantification of the body weight of control and *Chd8* cKO mice at different ages. Data are means ± SEM ($n = 4$–8 animals per genotype). ***G***, Whole-brain image (left) and coronal sections of control and *Chd8* cKO forebrain at P7 and P60 subjected to Nissl staining (right). Scale bars: 1 mm. ***H***, Quantification of total cortical thicknesses in control and *Chd8* cKO mice. Data are means ± SEM ($n = 3$ animals per genotype); $^{*}p < 0.05$, $^{**}p < 0.01$, $^{***}p < 0.001$; two-tailed unpaired Student's *t* test. ***I***, Representative images for the cerebellum, Pons, and hypothalamus (HT) of control and *Chd8* cKO animals. Scale bars: 1 mm.

To further examine autism-related behavioral abnormalities in *Chd8* cKO animals, we conducted the three-chamber test, the widely used test for general sociability and social interactions in mice (Kaidanovich-Beilin et al., 2011). In the initial three-chamber sociability analysis, control mice spent more time in the chamber with an unfamiliar mouse than a novel object, whereas *Chd8* cHet or *Chd8* cKO mice spent less time (Fig. 2*E*,*F*), suggesting that *Chd8*-deficiency in *Chd8* cHet and cKO mice impairs social preference. In the subsequent social novelty test, control and *Chd8* cHet mice spent more time in the chamber with a novel mouse than a familiar mouse, but *Chd8* cKO mice did not display preference for a novel mouse over a familiar mouse (Fig. 2*G*), suggesting that the *Chd8* cKO mice display attenuated preference for social novelty. Decreased exploratory behavior is consonant with increased anxiety, which is in line with the observations from the open field tests. This observation is in contrast to the previous report of *Emx1-Cre;Chd8*$^{fl/fl\text{-}Exon\text{-}3}$ mice showing decreased anxiety and increased preference for social novelty (Kweon et al., 2021), a discrepancy that is discussed later. Nonetheless, our observations that mice with *Chd8* ablation in the cortical progenitors exhibit increased anxiety-like behavior and reduced social preference are consistent with characteristic features observed in ASD (Frye, 2018; Hollocks et al., 2019).

Chd8 ablation in cortical NSCs leads to defects in cortical development and lamination

To determine the impact of *Chd8* ablation on cortical development, we analyzed the cortices of control and *Chd8* cKO mice at different developmental stages. Immunostaining with cortical layer-specific markers, such as CUX1 for the neurons in upper layers II–IV and CTIP2 for the neurons in deep layers V–VI (Molyneaux et al., 2007), showed a decrease in cortical thickness in *Chd8* cKO mice compared with controls (Fig. 3*A*). The upper cortical layers were substantially thinner, but the deep cortical neuronal layers were comparable to those of control mice at

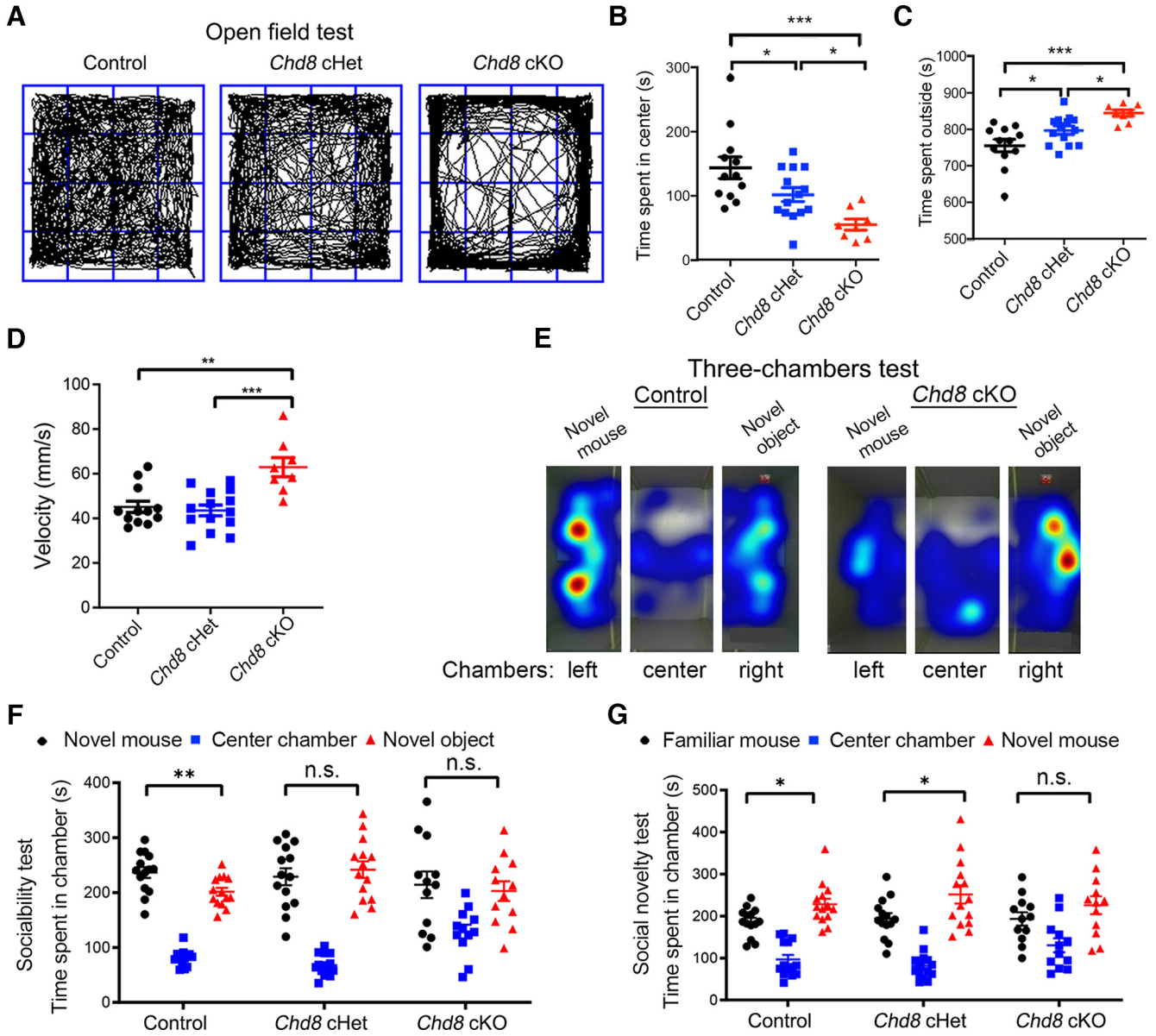

Figure 2. Mice with *Chd8* deletion in cortical neural stem cells exhibit abnormal behaviors. ***A–D***, Open field test for control, *Chd8* cHet, and *Chd8* cKO mice. Representative activity recordings (***A***), percentage of time spent in the central area (***B***), percentage of time spent outside the central area (***C***), movement velocity during the open field test (***D***). Data are means ± SEM (control, $n = 12$; *Chd8* cHet, $n = 14$; and *Chd8* cKO, $n = 8$); $^{*}p < 0.05$, $^{**}p < 0.01$, $^{***}p < 0.001$; one-way ANOVA followed by Tukey's multiple comparisons test. ***E***, Representative heat maps depicting dwell time in the three-chamber testing for control wild-type mice and *Chd8* cKO mice with novel unfamiliar mouse and object. ***F***, ***G***, Graphs depict the time spent in each chamber in the three-chamber socialization tests for control, *Chd8* cHet, and *Chd8* cKO mice (***F***) and time spent in in chambers with familiar and novel unfamiliar mice and the center chamber in the social novelty test (***G***). Data are means ± SEM (control, $n = 14$; *Chd8* cHet, $n = 14$; and *Chd8* cKO, $n = 12$); $^{*}p < 0.05$, $^{**}p < 0.01$, n.s., no significance, two-way ANOVA followed by Tukey's multiple comparisons test.

postnatal stages (Fig. 3*A–C*). Lamination in *Chd8* cKO mice was also disrupted as expression of the deep layer marker CTIP2 was observed in the upper cortical layers (Fig. 3*A*,*B*). No substantial defects were observed in layer-specific marker expression, cortical size, or the hippocampus in *Chd8* cHet mice (Fig. 3*D–G*). The loss of the upper-layer neurons, the population most responsible for callosal projections, also led to agenesis of the corpus callosum in *Chd8* cKO mice (Fig. 3*H*). Thus, *Chd8* deletion in the embryonic cortical NSCs leads to cortical malformations by disrupting cortical lamination and upper-layer neurons.

The decreased size of the cortex in *Chd8* cKO mice could be because of the defects in neural stem/progenitors. To interrogate this, we analyzed $PAX6^{+}$ stem-like RGC/NSC populations in the VZ/SVZ. In *Chd8* cKO mice, the number of $PAX6^{+}$ RGCs was lower at E12.5 than in control or *Chd8* cHet mice at the same stage (Fig. 4*A*). Similarly, at the neonatal stage P0, the $PAX6^{+}$ RGC population in the dorsal SVZ of *Chd8* cKO mice was substantially reduced (Fig. 4*B*), suggesting that CHD8 is required for the expansion of the RGC/NSC population in the developing cortex. Consistently, there was a substantial reduction in the number of M (mitosis) phase cells [marked by phosphorylated H3 (PH3)] in the VZ at E14.5 in *Chd8* cKO mice (Fig. 4*C*), whereas the number of $PH3^{+}$ cells was comparable between *Chd8* cHet and control mice (Fig. 4*D*), suggesting that proliferation of NSCs is compromised in the VZ of *Chd8* cKO animals. Similar results were observed using BrdU incorporation assays with the markers for $SOX2^{+}$ NSCs (Fig. 4*E*). To further examine the role of CHD8 in NSC proliferation, GFP^{+} cells were isolated from *Chd8* cKO carrying a Cre-dependent GFP reporter using FACS at E14.5 and subjected to a neurosphere formation assay

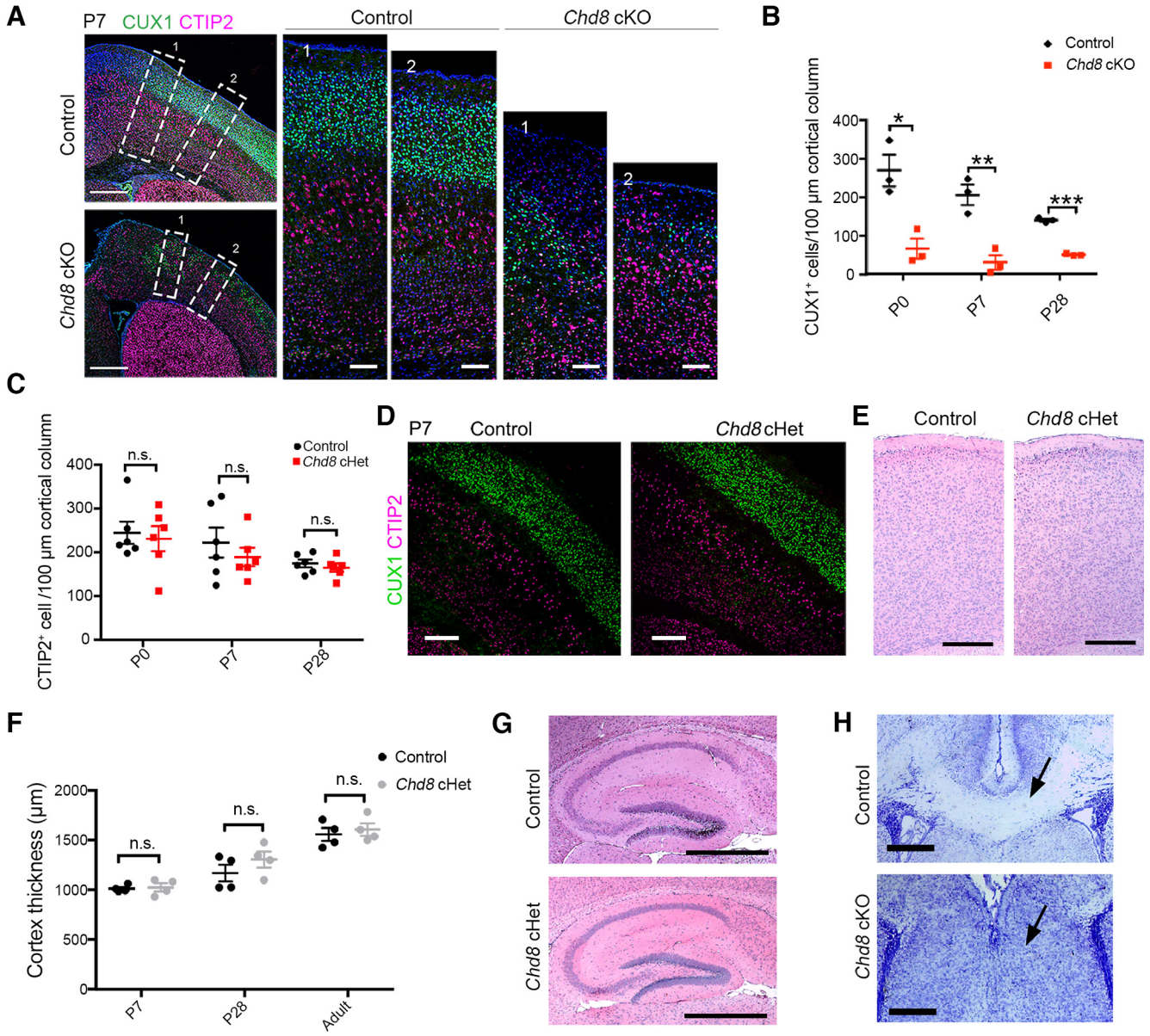

Figure 3. *Chd8* cKO, but not *Chd8* cHet, exhibit defects in cortical slamination. ***A***, Coronal sections of postnatal day (P)7 control (Emx1-Cre) and *Chd8* cKO forebrains immunostained for layer markers and DAPI (blue). Boxed areas in the left images are shown at a higher magnification in the corresponding images in the right. Scale bars: left, 500 μm; right, 100 μm. ***B***, Quantification of $CUX1^+$ cells per 100 μm column in cortices from control and *Chd8* cKO mice. Data are means ± SEM ($n = 3$ animals per genotype); $^*p < 0.05$, $^{**}p < 0.01$, $^{***}p < 0.001$; two-tailed unpaired Student's *t* test. ***C***, Quantification of $CTIP2^+$ cells per 100 μm column in cortices of control and *Chd8* cHet mice at indicated developmental stages. Data are means ± SEM ($n = 6$ animals per genotype); n.s., no significance, two-tailed unpaired Student's *t* test. ***D***, Coronal sections of P7 control and *Chd8* cHet mice immunostained for layer markers CUX1 and CTIP2. Scale bars: 100 μm. ***E***, Coronal sections of P28 cortex from control and *Chd8* cHet mice were subjected to HE staining. Scale bars: 200 μm. ***F***, Quantification of total cortical thicknesses in control and Chd8 cHet mice at different stages. Data are means ± SEM ($n = 4$ animals per genotype); n.s., no significance, two-tailed unpaired Student's *t* test. ***G***, Coronal sections of P28 hippocampus from control and *Chd8* cHet mice were subjected to HE staining. Scale bars: 1 mm. ***H***, Coronal sections of P7 forebrains from control and *Chd8* cKO mice were subjected to Nissl staining. Black arrows indicating the corpus callosum. Scale bars: 400 μm.

(Lu et al., 2016). The GFP^+ cells from *Chd8* cKO animals were defective in neurosphere growth (Fig. 4*F*,*G*). After passaging, *Chd8*-deficient cells formed neurospheres that were significantly smaller than those formed by VZ cells isolated from control mice (Fig. 4*G*). Together, these observations suggest that CHD8 is critical for NSC proliferation.

Chd8 loss results in precocious cell-cycle exit and defects in intermediate progenitor expansion

Given the defects in NSC proliferation in the VZ of *Chd8* cKO animals, we then investigated the effects of *Chd8*-deficiency on cell-cycle progression by performing sequential injections of IdU and BrdU at E14.5 (Fig. 5*A*). At the beginning of the experiment, pregnant mice were intraperitoneally injected with IdU to label a fraction of proliferative cells, followed by BrdU injection 1.5 h later to label synthesis (S) phase cells. After an additional 0.5 h, embryos were processed for immunostaining with antibodies specific for BrdU or IdU. In this system, cells labeled with IdU but not BrdU had left the S phase (Liu et al., 2015). We found that the percentage of cells that remained in the S phase (number of $BrdU^+$ cells divided by number of IdU^+ cells) was lower in the *Chd8* cKO cortices than in controls (Fig. 5*B*,*C*); however, the proportion of cells that had exited the S phase (number of IdU^+/BrdU-negative cells divided by number of IdU^+ cells) was higher in *Chd8* cKO embryos (Fig. 5*D*). In addition,

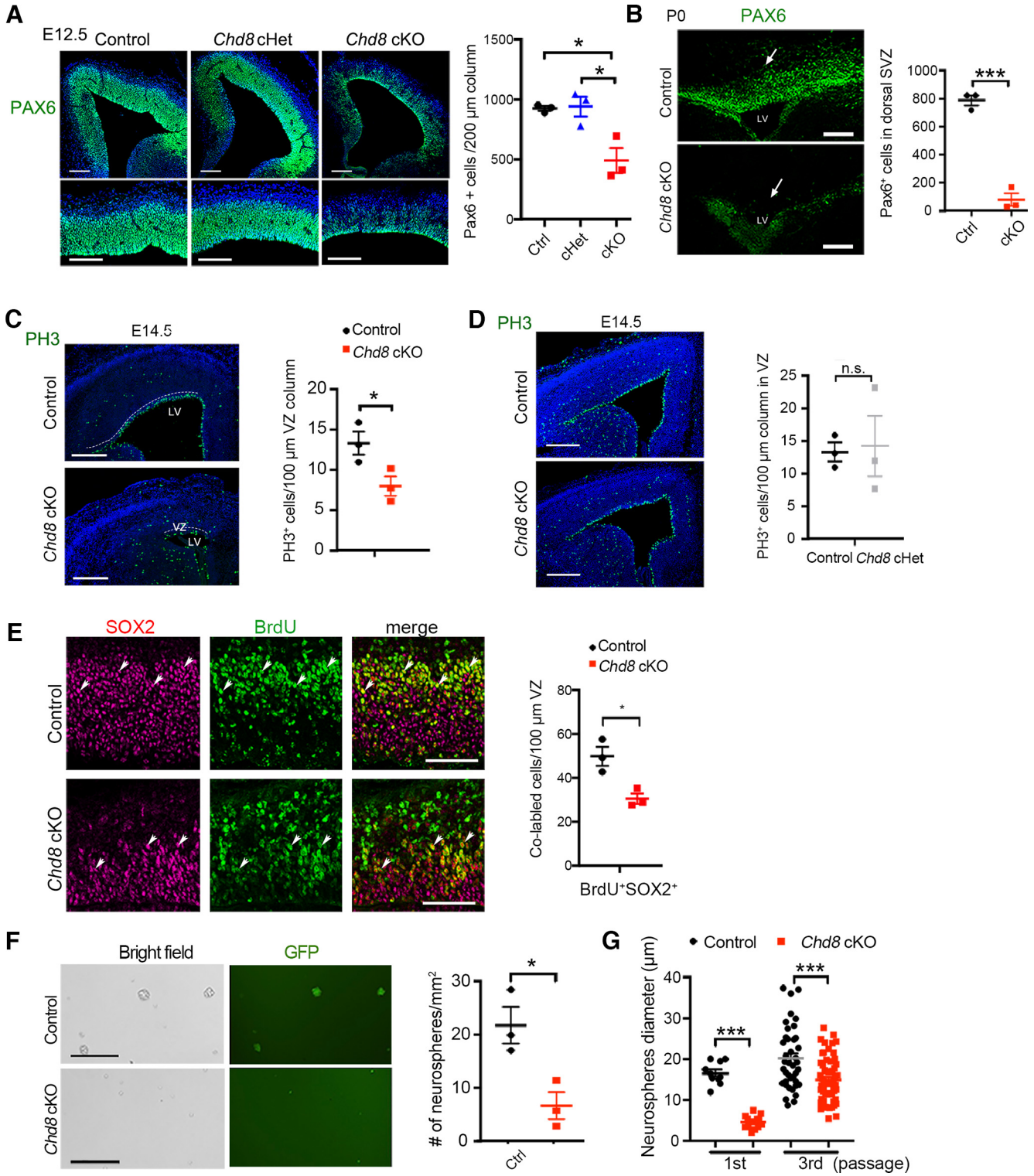

Figure 4. *Chd8* loss leads to defects in cortical progenitor cell proliferation. ***A***, Left, Coronal sections of E12.5 cortices of control, *Chd8* cHet, and *Chd8* cKO mice immunostained for radial glial marker PAX6 and DAPI (blue). Scale bars: 100 µm. Right, Quantification of the densities of $PAX6^+$ cells in the cortices of control, *Chd8* cHet, and *Chd8* cKO mice at E12.5. Data are means ± SEM ($n = 3$ animals per genotype); $^*p < 0.05$; one-way ANOVA followed by Tukey's multiple comparisons test. ***B***, Left, Coronal sections of postnatal day (P)0 brains of control and *Chd8* cKO mice immunostained for PAX6. Arrows indicate the SVZ. Scale bars: 100 µm. Right, Quantification of $PAX6^+$ cells in dorsal SVZ regions of control and *Chd8* cKO mice. Data are means ± SEM ($n = 3$ animals per genotype); $^{***}p < 0.001$; two-tailed unpaired Student's *t* test. ***C***, Left, Coronal sections of E14.5 cortices of control and *Chd8* cKO mice immunostained for phospho-H3 (PH3). Scale bars: 100 µm. DAPI, nuclei counterstain (blue), LV, lateral ventricle. Right, Quantification of $PH3^+$ cells in the VZ of control and *Chd8* cKO mice. Data are means ± SEM ($n = 3$ animals per genotype); $^*p < 0.05$; two-tailed unpaired Student's *t* test. ***D***, Left, Coronal sections of E14.5 control and *Chd8* cHet cortices immunostained for PH3. Scale bars: 200 µm. DAPI, nuclei counterstain (blue). Right, Quantification of $PH3^+$ cells in VZ of E14.5 control and *Chd8* cHet cortices. Data are means ± SEM ($n = 3$ animals per genotype); n.s., no significance, two-tailed unpaired Student's *t* test. ***E***, Left, Coronal sections of E12.5 brains of control and *Chd8* cKO mice immunostained for SOX2 and BrdU. Scale bars: 100 µm. BrdU administrated 2 h before mice were killed. Arrows indicated co-labeled cells. Right, Quantification of $BrdU^+SOX2^+$ cells in control and *Chd8* cKO mice. Data are means ± SEM ($n = 3$ animals per genotype); $^*p < 0.05$; two-tailed unpaired Student's *t* test. ***F***, Left, Images of NSCs isolated from cortices of E14.5 control and *Chd8* cKO mice cultured for 3 d. Scale bars: 100 µm. Right, Numbers of

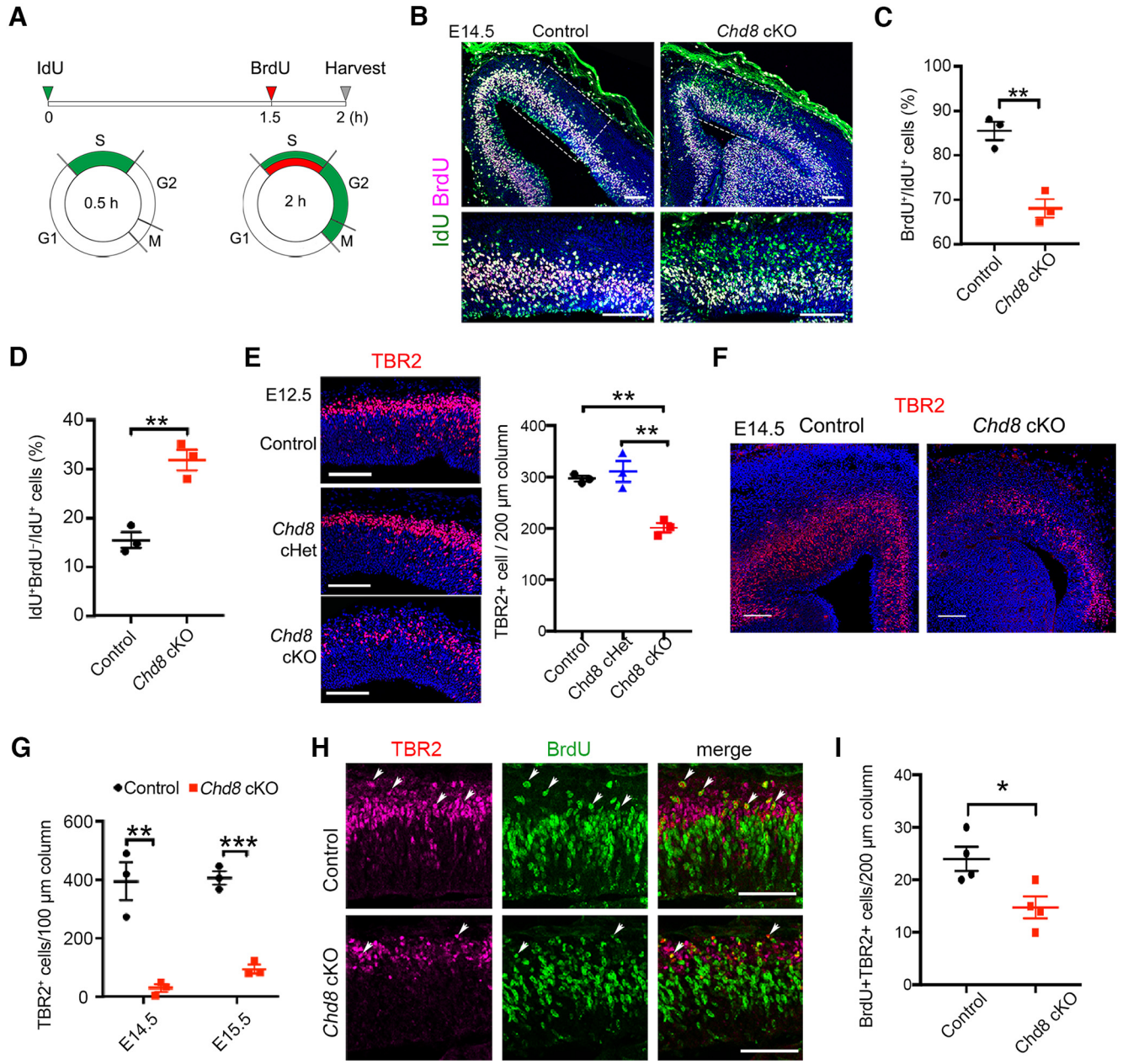

Figure 5. Deletion of CHD8 in cortical NSCs leads to IPCs proliferation defects and disruption of cell-cycle progression. ***A***, Schematic diagram of experimental design for IdU/BrdU injection and cell-cycle progression analysis. ***B***, Coronal sections of E14.5 cortices of control and *Chd8* cKO mice immunostained for IdU and BrdU. Boxed areas at top are shown at a higher magnification at bottom). Scale bars: 100 µm. DAPI, nuclei counterstain (blue). ***C***, Percentage of $IdU^+/BrdU^+$ S phase cells in cortices of control and *Chd8* cKO mice. Data are means ± SEM ($n = 3$ animals/group); $^{**}p < 0.01$; two-tailed unpaired Student's *t* test. ***D***, Percentage of $IdU^+/BrdU^-$ cells that have exited S phase in cortices of control and *Chd8* cKO mice. Data are means ± SEM ($n = 3$ animals/group); $^{**}p < 0.01$; two-tailed unpaired Student's *t* test. ***E***, Left, Coronal sections of E12.5 cortices of control, *Chd8* cHet, and *Chd8* cKO mice immunostained for IPC marker TBR2 and DAPI (blue). Scale bars: 100 µm. Right, Quantification of the densities of $TBR2^+$ cells in the cortices of control, *Chd8* cHet, and *Chd8* cKO mice at E12.5. Data are means ± SEM ($n = 3$ animals per genotype); $^{**}p < 0.01$; one-way ANOVA followed by Tukey's multiple comparisons test. ***F***, Coronal sections of E14.5 cortices of control and *Chd8* cKO mice immunostained for TBR2 and DAPI (blue). Scale bars: 200 µm. ***G***, Quantification of $TBR2^+$ cells per 100 µm areas of VZ of control and *Chd8* cKO mice at E14.5 and E15.5. Data are means ± SEM ($n = 3$ animals per genotype); $^{**}p < 0.01$, $^{***}p < 0.001$; two-tailed unpaired Student's *t* test. ***H***, Cortical regions of E14.5 control and *Chd8* cKO immunostained for BrdU and TBR2. Scale bars: 100 µm. BrdU administrated 2 h before mice were killed. Arrows indicated co-labeled cells. ***I***, Quantification of $BrdU^+TBR2^+$ cells in E14.5 control and *Chd8* cKO cortices. Data are means ± SEM ($n = 3$ animals per genotype); $^{*}p < 0.05$; two-tailed unpaired Student's *t* test.

←

neurospheres from the first passage of NSCs isolated from control and *Chd8* cKO cortices. Data are means ± SEM ($n = 3$ independent experiments per genotype); $^{*}p < 0.05$; two-tailed unpaired Student's *t* test. ***G***, Diameters of neurospheres from first and third passages of NSCs from control and *Chd8* cKO mice. Data are means ± SEM ($n = 3$ independent experiments per genotype); $^{***}p < 0.001$; two-tailed unpaired Student's *t* test.

more IdU^+/BrdU-negative cells had migrated into the cortical mantle zone in *Chd8* cKO mice than control (Fig. 5*B*), suggesting a precocious cell-cycle exit of *Chd8* cKO NPCs.

Consistently, the number of $TBR2^+$ IPCs, which are basal progenitors in the SVZ essential for mammalian neocortical expansion (Lui et al., 2011; Florio and Huttner, 2014), were substantially lower in the *Chd8* cKO at E12.5 (Fig. 5*E*) and at later

stages (e.g., E14.5 and E15.5) than control or *Chd8* cHet animals (Fig. 5*F*,*G*). Moreover, BrdU pulse-labeling assays indicated that the proliferation of IPC cells ($BrdU^+TBR2^+$) was substantially reduced in the *Chd8* cKO cortex (Fig. 5*H*,*I*). Together, these data suggest that precocious cell-cycle exit caused by CHD8 loss contributes to a defect in IPC proliferation and expansion during cortical development.

Temporally induced ablation reveals a stage-specific requirement of CHD8 for NSC and IPC survival

The decreased number of NSCs and IPCs in the VZ and SVZ, respectively, in the *Chd8* cKO animals prompted us to analyze apoptotic events in the developing cortex. We immunostained cortices from different developmental stages with a marker for apoptotic cells, cleaved caspase 3 (C-Casp3). We detected massive $C\text{-}Casp3^+$ cells in the cortices of *Chd8* cKO mice beginning at E11.5, peaking at E12.5 (Fig. 6*A*). However, we found that the cell death was nearly absent in the *Chd8* cKO cortex after E14.5 (Fig. 6*A*). Next, we sought to determine the progenitor cell types undergoing apoptosis and found that C-Casp3 expression was predominantly in $PAX6^+$ NPCs and $TBR2^+$ IPCs in the VZ and SVZ of the *Chd8* cKO cortex at E12.5 (Fig. 6*B*,*C*), as well as in $TUJ1^+$ postmitotic neurons to a lesser extent (Fig. 6*D*). This observation is in contrast to the minimal cell death previously reported in $PAX6^+$ RGCs/NPCs in *Emx1-Cre;Chd8*$^{fl/fl\text{-}Exon\text{-}3}$ embryos (Kweon et al., 2021). However, C-Casp3 was barely detectable in the cortices of control or *Chd8* cHet animals at these stages (Fig. 6*A*). These data suggest that RGC/NPC and IPC cell death occurs predominantly in the *Chd8* cKO cortices.

Consistent with a proposed role of CHD8 for p53-mediated apoptosis (Nishiyama et al., 2009), we found that p53 expression was upregulated in the developing cortex of *Chd8* cKO mice at E11.5 and increased at E12.5 but was essentially undetectable at E14.5 (Fig. 6*E*). Similarly, expression of the downstream targets of p53 signaling, such as *p21* and *Sesn2,* was increased at E12.5 in the *Chd8* cKO cortices compared with control cortices (Fig. 6*F*). Activation of the p53 signaling pathway is often induced by DNA damage with double-strand breaks (Williams and Schumacher, 2016). We therefore immunostained the cortices with a DNA damage response marker, γH2AX, and observed higher levels of γH2AX in the cortices of *Chd8* cKO mice at E12.5 compared with controls (Fig. 6*G*), suggesting that CHD8 loss leads to DNA damage, which may in turn cause the progenitor death.

To further determine the specific time window during which CHD8 is required for cortical progenitor population survival, we then used a tamoxifen-inducible Nestin-Cre^{ERT2} line (Imayoshi et al., 2006) to generate *Chd8*$^{fl/fl}$;*Nestin-Cre*$^{ERT2+/-}$ mice (referred to here as *Chd8* iKO mice). *Chd8* ablation was induced by tamoxifen administration at different embryonic stages (Fig. 6*H*). Ablation of *Chd8* at E10.5 and E11.5 in *Chd8* iKO mice, which were harvested at E13.5 and E14.5, respectively, led to extensive apoptosis in the cortex as indicated by C-Casp3 immunostaining (Fig. 6*I*,*J*). C-Casp3 and p53 were also upregulated in the same cells in the cortex of *Chd8*-iKO mice (Fig. 6*K*). In contrast, *Chd8* ablation after E13.5 did not result in detectable C-Casp3 expression in the cortical region (Fig. 6*I*,*J*), suggesting a stage-specific impact of CHD8 loss on neural progenitor cell survival.

Given that $TBR2^+$ IPCs are generated and expanded predominantly between E11.5 and E13.5 during cortical development (Sessa et al., 2008; Vasistha et al., 2015), we then examined whether *Chd8* ablation results in IPC cell death at different embryonic stages. Strikingly, we observed a substantial increase of apoptosis in a population of $TBR2^+$ IPCs at E14.5 when CHD8 is ablated at E11.5 but not at other stages (Fig. 6*L*,*M*), suggesting that CHD8 is critical for the survival of the intermediate progenitor IPCs. Because the generation of neurons in the upper cortical layers stems predominantly through IPCs (Sessa et al., 2008; Kriegstein and Alvarez-Buylla, 2009), the cell death of IPCs caused by CHD8 loss during embryonic neurogenesis likely contributes to the reduction of $CUX1^+$ upper-layer cortical neurons in *Chd8* cKO animals. Together, our data reveal a stage-specific role of CHD8 for the survival of NSCs and IPCs during cortical neurogenesis.

p53-dependent and p53-independent roles of CHD8 in cortical progenitor survival and development

Given that upregulation of p53 in developing *Chd8* cKO cortices could trigger cell death, we next asked whether inhibition of p53 could block apoptosis and restore neurogenesis during cortical development. We crossed *Chd8*$^{fl/fl}$ mice with *Trp53*$^{fl/fl}$ and *Emx1-Cre* mice to ablate both *Chd8* and *p53* in *Emx1*-expressing cortical NSCs [referred to as *Chd8*; *p53* double KO (dKO) mice]. In cortices of *Chd8* cKO animals heterozygous for p53 knockout (referred to as *Chd8* cKO; *p53* cHet), numbers of $C\text{-}Casp3^+$ cells were reduced compared with *Chd8* cKO animals (Fig. 7*A*,*B*). This is consistent with the observation in *Sox1-Cre*;*Chd8* cKO-p53 heterozygous embryos (Hurley et al., 2021). Moreover, we found that C-Casp3 signals were essentially absent in cortices of *Chd8*;*p53* dKO animals (Fig. 7*A*,*B*). This suggests that p53 ablation rescues, if not fully, the apoptotic phenotype in the *Chd8*-deficient cortex during early development. Next, we sought to address whether the proliferative capacity of NSCs was restored by p53 ablation. We found that the number of $PH3^+$ proliferative cortical NSCs was higher in *Chd8*;*p53* dKO and *Chd8* cKO;*p53*cHet mice compared with *Chd8* cKO mice at E14.5 (Fig. 7*C*,*D*), but lower than that of controls. This suggests that the rescue of the apoptotic phenotype does not fully restore the NSC proliferation defects in the cortex of *Chd8* cKO mice. Similarly, the number of $TBR2^+$ IPCs in *Chd8*;*p53* dKO mice was also lower compared with the control, despite an increase compared with that of *Chd8* cKO or *Chd8* cKO;*p53* cHet mice (Fig. 7*E*,*F*). These observations suggest that blocking apoptosis caused by p53 downregulation does not fully rescue the defects in NSC proliferation and IPC production in *Chd8*-deficient embryos, indicative of a p53-independent role for CHD8 in cortical progenitor cell development.

CHD8 targets neurogenesis-associated genes to control cortical development

To determine the potential mechanisms underlying CHD8 function in neurogenesis, we performed transcriptome profiling of $GFP\ reporter^+$ cells that FACS isolated from control and *Chd8* cKO cortices at E14.5. There were ~480 downregulated and ~204 upregulated genes in *Chd8* cKO compared with control cells (FDR < 0.1, $p < 0.01$; Fig. 8*A*). Gene ontology analysis of the differentially expressed genes revealed that downregulated genes were involved in processes related to neurogenesis, neuron differentiation, neural precursor cells proliferation, and axon development (Fig. 8*A*–*C*), which may contribute to the cortical dysgenesis phenotype observed in *Chd8* cKO mice. In contrast, the upregulated genes were predominantly associated with apoptotic and p53 pathways (Fig. 8*B*,*C*).

To determine whether CHD8 directly regulates expression of these differentially expressed genes, we integrated our transcriptomic data with CHD8 binding sites in the embryonic cortex identified by ChIP-seq (Katayama et al., 2016) along with

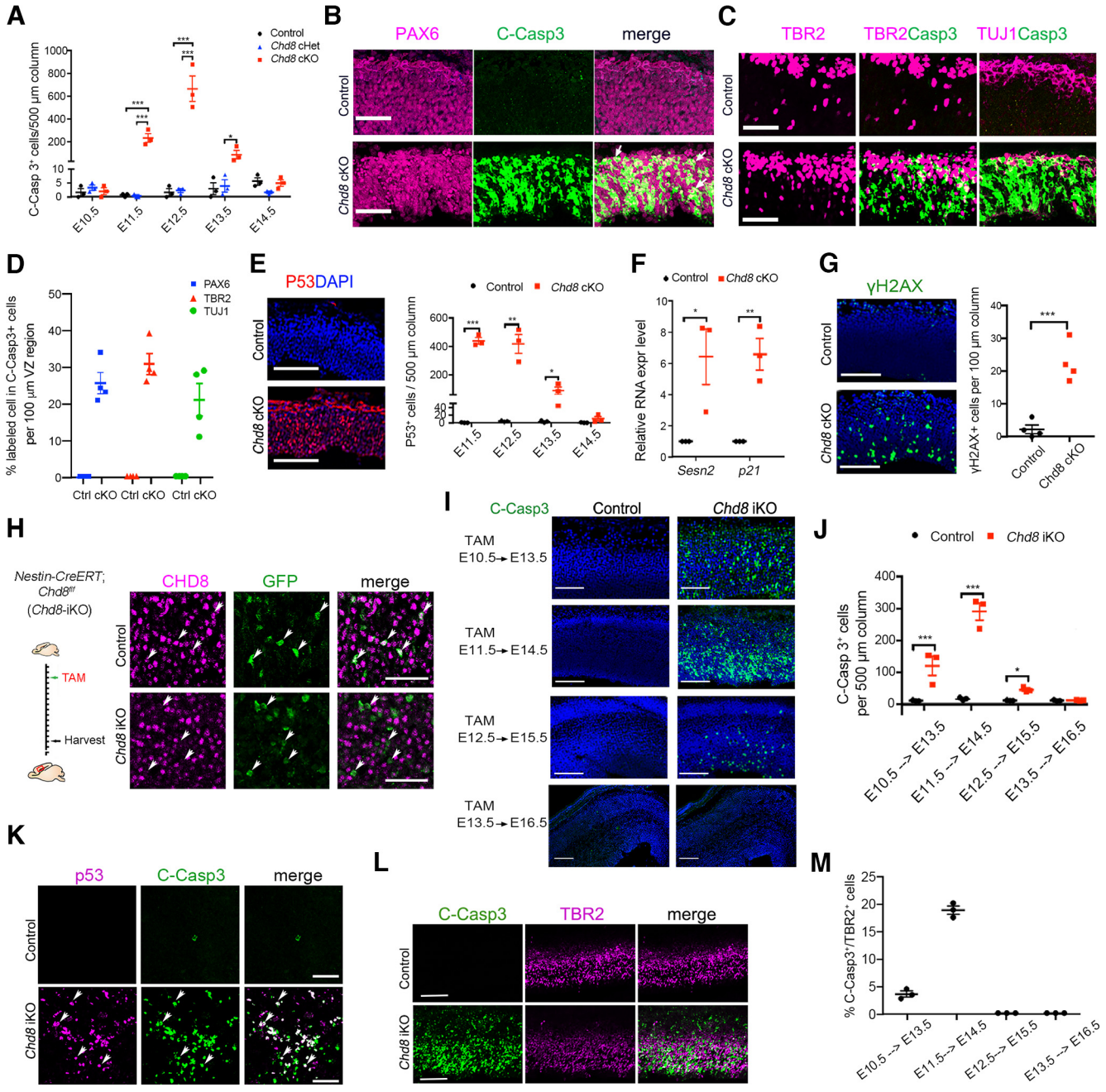

Figure 6. Temporally specific effects of *Chd8* loss on NPC and IPC apoptosis and p53 upregulation at early embryonic stages. ***A***, Quantification of C-Casp3$^+$ cells from control, *Chd8* cHet, and *Chd8* cKO mice. Data are means ± SEM ($n = 3$ animals per genotype); ***$p < 0.001$; two-way ANOVA followed by Tukey's multiple comparisons test. ***B***, ***C***, Coronal sections of cortices from E12.5 control and *Chd8* cKO mice immunostained for C-Casp3 and PAX6 (***B***), TBR2, or TUJ1 (***C***). Scale bars: 50 µm. Arrows indicate the colabeled cells. ***D***, Percentage of PAX6, TBR2, and TUJ1 in C-Casp3$^+$ cells in control and *Chd8* cKO mice. Data are means ± SEM ($n = 4$ animals/group). ***E***, Left, Coronal sections of cortices from control and *Chd8* cKO mice immunostained for p53. Scale bars: 100 µm. DAPI, nuclei counterstain (blue). Right, Quantification of p53$^+$ cells per 500 µm cortical column from control and *Chd8* cKO mice. Data are means ± SEM ($n = 3$ animals/group); *$p < 0.05$, **$p < 0.01$, ***$p < 0.001$; two tailed unpaired Student's *t* test. ***F***, qRT-PCR analysis of *Sesn2* and *p21* in E12.5 control and *Chd8* cKO cortices. Data are means ± SEM ($n = 3$ animals per genotype); *$p < 0.05$, **$p < 0.01$; two-tailed unpaired Student's *t* test. ***G***, Left, Coronal sections of E12.5 forebrains of control and *Chd8* cKO mice immunostained for γH2AX. Scale bars: 100 µm. DAPI, nuclei counterstain (blue). Right, Quantification of γH2AX $^+$ cells per 100 µm cortical column from control and *Chd8* cKO mice. Data are means ± SEM ($n = 4$ animals/group); ***$p < 0.001$; two tailed unpaired Student's *t* test. ***H***, Left, schematic representation of tamoxifen administration to Nestin-CreERT;*Chd8* iKO mice. Right. Immunostaining for the GFP reporter and CHD8 on the control and *Chd8* iKO $^{CC\text{-}GFP}$ cortex at E14.5, tamoxifen was administrated at E11.5. Arrows indicate the GFP$^+$ cells. Scale bars: 50 µm. ***I***, Coronal sections of control and *Chd8* iKO cortices immunostained for C-Casp3 and DAPI (blue). Scale bars: 200 µm. ***J***, Quantification of C-Casp3$^+$ cells from forebrains of control and *Chd8* cKO mice. Data are means ± SEM (n = 3 animals/group); *$p < 0.05$; ***$p < 0.001$; two-tailed unpaired Student's *t* test. ***K***, The cortex of control and *Chd8* iKO mice were immunostained for p53 and C-Casp3 at E14.5 after tamoxifen administration at E11.5. Scale bars: 50 µm. Arrows indicated co-labeled cells. ***L***, Coronal sections of control and *Chd8* iKO cortices at E14.5 after TAM administration at E11.5 were immunostained for C-Casp3 and TBR2. Scale bars: 200 µm. ***M***, Percentage of C-Casp3$^+$ TBR2$^+$ cells in TBR2$^+$ cells ($n = 3$ animals/group). Data are means ± SEM.

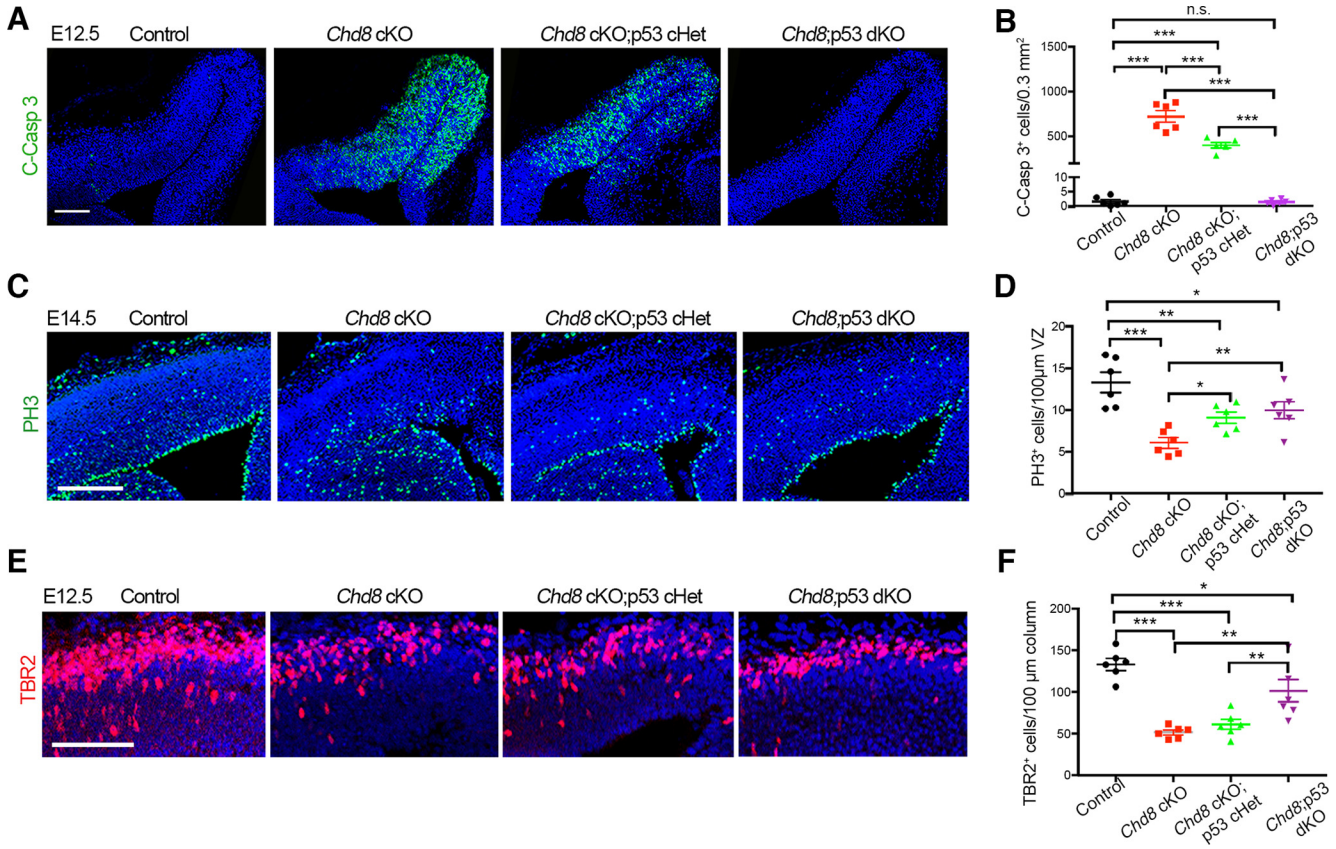

Figure 7. Deletion of p53 partially rescues the phenotype in *Chd8* deficient mice. ***A***, Coronal sections of E12.5 cortices from control, *Chd8* cKO, and *Chd8* cKO animals heterozygous for p53 knock-out (*Chd8* cKO; *p53* cHet), and *Chd8*; *p53* dKO mice immunostained for C-Casp3. Scale bar, 100 μm. DAPI, nuclei counterstain (blue). ***B***, Quantification of C-Casp3$^+$ cells from control, *Chd8* cKO, *Chd8* cKO; *p53* cHet, and *Chd8; p53* dKO mice. Data are means ± SEM ($n = 6$ animals per genotype); $^{***}p < 0.001$, n.s., no significance; one-way ANOVA followed by Tukey's multiple comparisons test. ***C***, Coronal sections of E14.5 cortices from control, *Chd8* cKO, *Chd8* cKO; *p53* cHet, and *Chd8*; *p53* dKO mice immunostained for PH3. Scale bar, 200 μm. ***D***) Quantification of PH3$^+$ cells in VZ region from cortices of control, *Chd8* cKO, *Chd8* cKO; *p53* cHet, and *Chd8*; *p53* dKO mice. Data are means ± SEM ($n = 6$ animals per genotype); $^*p < 0.05$, $^{**}p < 0.01$, $^{***}p < 0.001$; one-way ANOVA followed by Tukey's multiple comparisons test. ***E***, Coronal sections of E14.5 cortices from control, *Chd8* cKO, *Chd8* cKO; *p53* cHet, and *Chd8*; *p53* dKO mice immunostained for TBR2, Scale bar, 200 μm. ***F***, Quantification of TBR2$^+$ cells from cortices of control, *Chd8* cKO, *Chd8* cKO; *p53* cHet, and *Chd8*; *p53* dKO mice. Data are means ± SEM ($n = 6$ animals per genotype); $^*p < 0.05$, $^{**}p < 0.01$, $^{***}p < 0.001$; one-way ANOVA followed by Tukey's multiple comparisons test.

H3K27ac and H3K4me3 associated with enhancers and promotors, respectively (Platt et al., 2017; Zhao et al., 2018). CHD8 binding sites overlapped considerably with those of the activating histone marks H3K4me3 and H3K27ac, but not the repressive histone mark H3K27me3 (Fig. 8*D*), suggesting that CHD8 is associated with active promotor or enhancer elements to activate target gene expression. Among the differentially regulated genes in *Chd8* cKO cortices, ~435 gene loci had CHD8 binding sites in their promoter/enhancer regions (Fig. 8*E*). Gene enrichment analysis indicated that CHD8 directly targets the gene loci related to neurogenesis and NPC proliferation among the downregulated genes in *Chd8* cKO cortices (Fig. 8*F*,*G*). In particular, CHD8 targeted the regulatory elements of a set of neurogenesis-promoting genes including *Tbr2/Eomes*, which encodes a key regulator of IPC-mediated indirect neurogenesis, and *Emx2*, *Lhx2*, *Neurg2*, *Neurod1*, and *Nefl*, as well as those with NPC proliferation, for example, *Nes*, *Lef1*, *Ltbp3*, and *Crb2* (Fig. 8*F*,*G*). These data suggest that CHD8 may directly target and activate expression of NSC- and neurogenesis-associated genes including IPC-neurogenic regulators for cortical neurogenesis.

CHD8 is critical for maintaining chromatin accessibility landscape for cortical neurogenesis

CHD8 is an ATP-dependent chromatin remodeler, and thus we hypothesized that CHD8 regulates transcription of neurogenesis-related genes by controlling chromatin accessibility. To evaluate chromatin accessibility, we used ATAC-seq (Buenrostro et al., 2015) to compare open chromatin regions in the GFP$^+$ cells isolated from *Chd8* cKO and control cortical tissues at E14.5. We detected an extensive alteration of ATAC-seq signals in *Chd8*-ablated cells. The number of accessible open chromatin sites appeared to be substantially lower in *Chd8*-ablated cells compared with control cells (Fig. 8*H*,*I*), whereas there was a modest decrease in the ATAC-seq peak signals in *Chd8* cHet NPCs (Fig. 8*I*).

Pathway enrichment analysis indicated that the gene loci with decreased accessibility were enriched in neural differentiation, cell cycle/mitosis, DNA repair, WNT signaling, and Hedgehog signaling pathways (Fig. 8*J*). Consistent with transcriptome profiling, chromatin accessibility was decreased in critical neurogenesis-promoting regulatory genes including *Neurod1*, *Tbr2/Eomes*, and *Fezf2*, as well as neural progenitor proliferation-related genes including *Nes*, *Smarcd3*, and *Fzd9* (Fig. 8*K*), the expression of which was also downregulated in *Chd8* cKO cortices (Fig. 8*C*). In addition, qRT-PCR analysis validated the downregulation in the expression levels of these genes in *Chd8* cKO cortices compared with controls (Fig. 8*L*). These results suggest that CHD8 is required for maintaining the proper chromatin landscape of key regulatory genes important for cortical progenitor proliferation and differentiation.

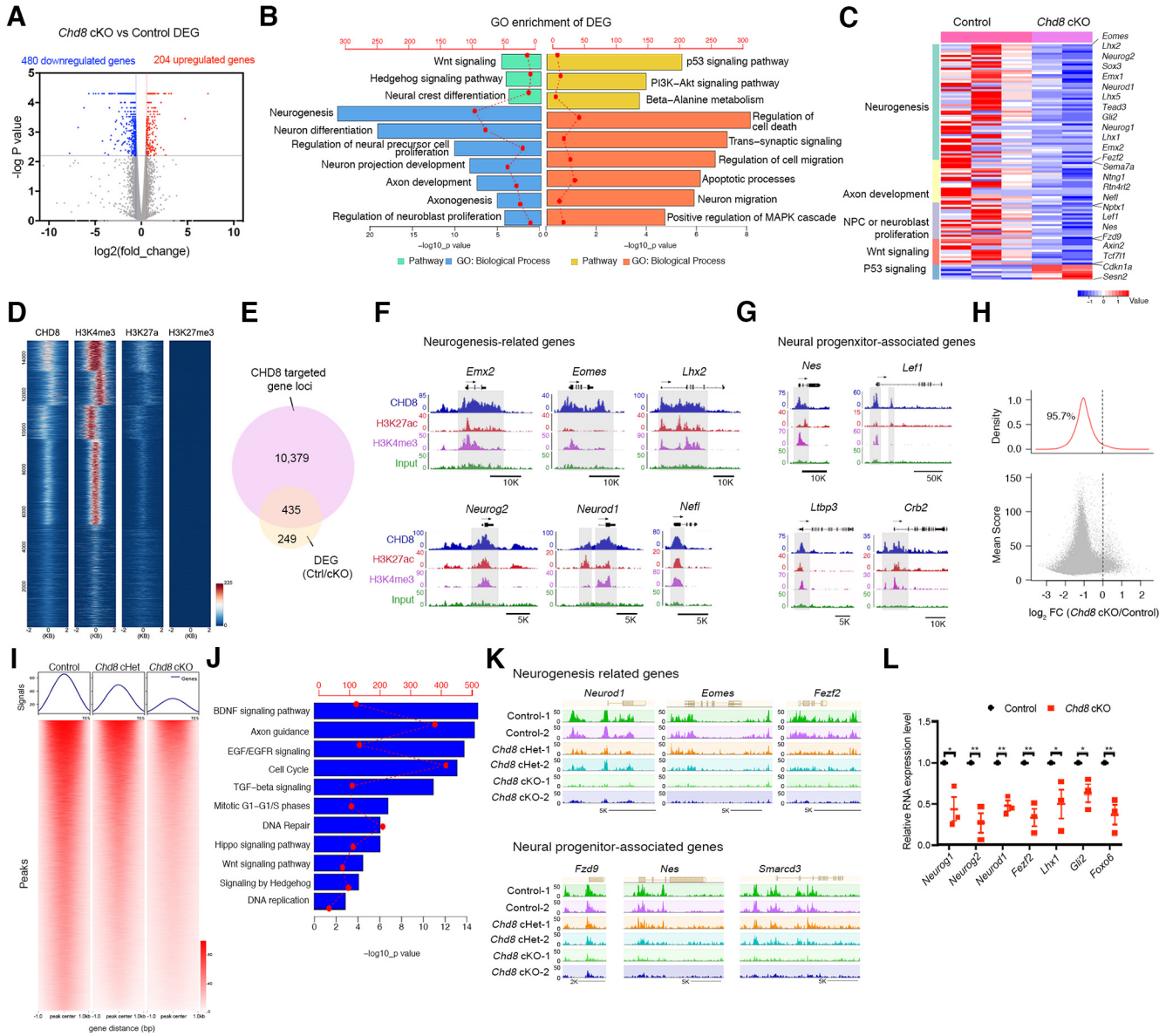

Figure 8. CHD8 maintains proper chromatin landscape and regulates neurogenesis-related genes to control cortical development. ***A***, Volcano plot of differentially expressed genes (DEG) from transcriptome profiles of the GFP$^+$ reporter cells isolated from E14.5 Emx1-Cre control ($n = 3$) and *Chd8* cKO ($n = 2$) cortices. Blue and red dots represent genes downregulated and upregulated, respectively, in *Chd8* cKO cortices (FDR < 0.1, FDR-corrected p value < 0.01, fold change > 1.5). ***B***, Gene ontology analysis of significantly downregulated (left) and upregulated (right) genes in *Chd8* cKO cortices. ***C***, Heat map of categories of differentially expressed genes in control and *Chd8* cKO cortices. ***D***, Heat map of ChIP-seq data for CHD8, H3K4me3, H3K27ac, and H3K27me3 in E14.5 mouse cortices. ***E***, Venn diagram of differentially expressed genes and gene loci bound by CHD8. ***F***, ***G***, Representative CHD8, H3K27ac, and H3K4me3 tracks of neurogenesis-related genes (***E***) and genes involved in neural precursor cell proliferation (***F***). ***H***, Changes of chromatin accessibility in *Chd8* wild-type control and *Chd8* KO FACS-sorted cells. Bottom, Each dot represents one ATAC-Seq peak. Top, Percentage of reduced peaks. ***I***, Heat map plots of average ATAC-seq peak signals in *Chd8* wild-type control, *Chd8* cHet and *Chd8* cKO FACS-sorted cells ($n = 2$ samples/genotype). Each row represents one peak. The color intensity indicates chromatin accessibility. ***J***, Pathway enrichment of genes with decreased chromatin accessibility in *Chd8* cKO FACS-sorted cells compared with controls. ***K***, Representative ATAC-seq tracks of neurogenesis-related genes downregulated in *Chd8* cKO FACS-sorted cells compared with control and *Chd8* cHet cells ($n = 2$ samples/genotype). ***L***, qRT-PCR analysis of neurogenesis-related genes in E14.5 control and *Chd8* cKO cortices. Data are means ± SEM ($n = 3$ animals/genotype); *$p <$ 0.05, **$p < 0.01$; Student's t test.

CHD8 loss impedes neurogenesis from NSCs in the adult SVZ

Although ASD is generally thought of as a neurodevelopmental disease, adults can present with ASD symptoms (Bernier et al., 2014; Courchesne et al., 2019). CHD8 remains expressed in the NPCs in adult neurogenic regions in the SVZ and SGZ as indicated by colabeling of CHD8 with the markers for adult neural stem/progenitor cells, Nestin and SOX2 (Fig. 9*A*,*B*). Notably, adult *Chd8* cKO mice exhibited forebrain and hippocampal dysgenesis (Figs. 1*G*, 9*C*), suggesting a potential role for CHD8 in adult neurogenesis. In adult mice, newly formed neurons are generated from transit-amplifying IPCs in the SVZ and then migrate into the olfactory bulb through the rostral migratory stream (RMS; Ming and Song, 2011). To investigate the effect of CHD8 loss on adult neurogenesis, we treated adult *Chd8* iKO mice carrying the inducible NSC-expressing *Nestin-Cre*^{ERT2} line TAM for 5 d to ablate *Chd8* and labeled dividing NSCs with BrdU 4 weeks post-TAM, in which BrdU will also label newborn neurons from NSCs subsequently (Lagace et al., 2007; Fig. 9*D*). *Chd8* ablation was confirmed in the GFP reporter$^+$ cells by immunohistochemistry (Fig. 9*E*). Newborn neurons labeled with BrdU were reduced in the olfactory bulbs of *Chd8* iKO mice

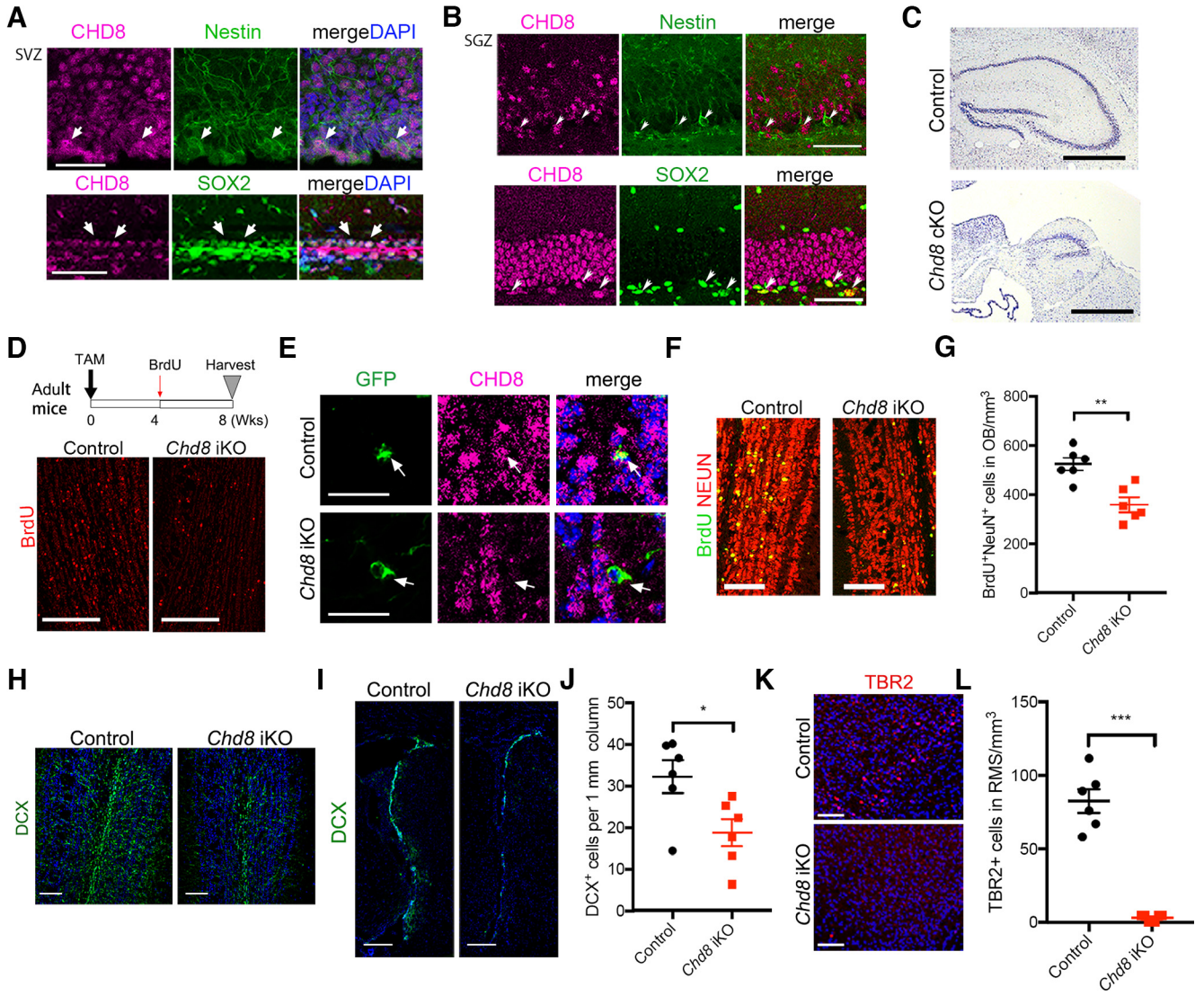

Figure 9. CHD8 is required for adult neurogenesis from the SVZ progenitors in the forebrain. ***A***, ***B***, The SVZ (***A***) and SGZ (***B***) of adult wild-type mice immunostained for CHD8, SOX2, and Nestin. White arrows indicate colabeled cells. Scale bars: 100 μm. DAPI, nuclei counterstain (blue). ***C***, The hippocampus of WT control and *Chd8* cKO mice at postnatal day (P)60 subjected to Nissl staining. Scale bars: 1 mm. ***D***, Top, Schematic diagram of experimental design of tamoxifen treatment and BrdU injection. Wks, Weeks Bottom, Representative images of olfactory bulb coronal sections of control (Nestin-CreERT) and *Chd8* iKO adult mice ($n = 6$ animals/genotype) injected with BrdU immunostained for BrdU; Scale bars: 200 μm. ***E***, Coronal sections of olfactory bulbs of adult control and *Chd8* iKO mice immunostained for GFP reporter and CHD8. White arrows indicate cells that express GFP. Scale bars: 40 μm. DAPI, nuclei counterstain (blue). ***F***, ***G***, Coronal sections of olfactory bulbs of adult control and *Chd8* iKO mice injected with TAM and BrdU immunostained for BrdU and NEUN (***F***) and quantification of $BrdU^+/NEUN^+$ cell numbers (***G***). Data are means ± SEM ($n = 6$ animals/genotype); $^{**}p < 0.01$; two-tailed unpaired Student's *t* test. Scale bars: 100 μm. ***H***, ***I***, Coronal sections of olfactory bulbs (***H***) and SVZ regions (***I***) from adult control and *Chd8* iKO mice injected with TAM and immunostained for immature neuron marker DCX. Scale bars: ***H***, 100 μm; ***I***, 200 μm. DAPI, nuclei counterstain. ***J***, Quantification of DCX^+ cell numbers in SVZ regions of adult control and *Chd8* iKO mice. Data are means ± SEM ($n = 6$ animals per genotype); $^{*}p < 0.05$; two-tailed unpaired Student's *t* test. ***K***. Sagittal section of RMS regions from adult control and *Chd8* iKO mice treated with TAM and immunostained for TBR2. Scale bars: 100 μm. DAPI, nuclei counterstain (blue). ***L***, Quantification of $TBR2^+$ cell numbers in RMS regions of adult control and *Chd8* iKO mice. Data are means ± SEM ($n = 6$ animals/genotype); $^{***}p < 0.001$; two-tailed unpaired Student's *t* test.

compared with control mice (*Nestin-Cre*^{ERT2}; Fig. 9*D*). Colabeling with the mature neuronal marker NeuN revealed a significant reduction in the newborn neuronal population in *Chd8* iKO mice (Fig. 9*F*,*G*). Moreover, the number of DCX^+ neuroblasts was lower in the olfactory bulbs and the SVZ of *Chd8* iKO mice than controls (Fig. 9*H–J*). Strikingly, $TBR2^+$ IPCs in the RMS region in the forebrain were substantially reduced in *Chd8* iKO mice (Fig. 9*K*,*L*), suggesting that depletion of CHD8 impedes IPC production during adult neurogenesis.

In contrast to the developing cortex at early embryonic stages, we did not detect any significant alteration in the number of proliferative cells assayed by Ki67 expression or BrdU incorporation, as well as cell death assayed by activated Caspase-3 or p53 expression in the SVZ of adult *Chd8* iKO brains (Fig. 10*A–D*). These observations suggest that CHD8 deletion does not substantially affect adult NSC proliferation and survival in the adult brain but impairs the production of DCX^+ IPCs or neuroblasts.

The presence of reduced newborn neurons in the *Chd8* iKO olfactory bulb suggests that the neurogenesis deficit is likely not because of migration defects but instead because of a defect of differentiation from NSCs in the SVZ. Adult NSCs from the SVZ can differentiate into different types of neurons in the olfactory bulb including CB^+ and TH^+ cells (Merkle et al., 2007). Consistently, we found that numbers of both newly generated CB^+ and TH^+ interneurons labeled by BrdU and NeuN decreased in the olfactory bulb of *Chd8* iKO mice compared

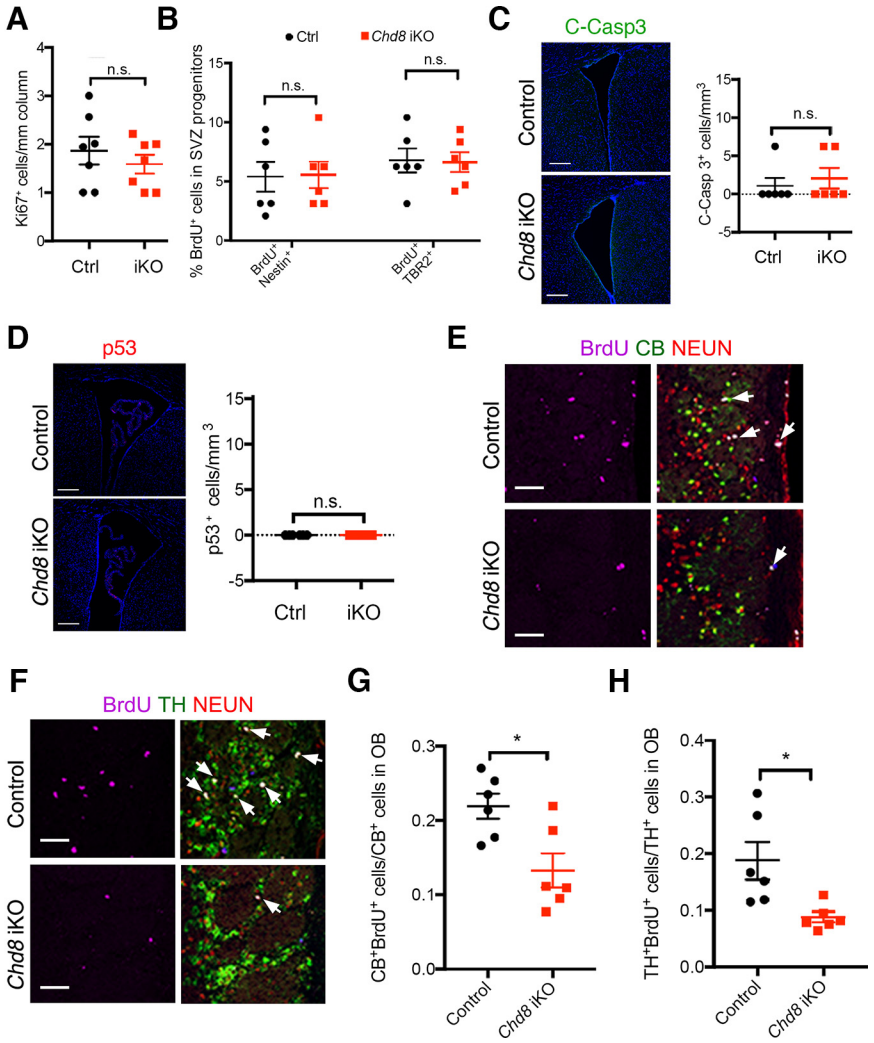

Figure 10. *Chd8* ablation impairs neural differentiation from adult NSCs but not their survival. ***A***, Quantification of Ki67$^+$ cells in the SVZ region from adult control and *Chd8* iKO mice. Data are means ± SEM ($n = 7$ animals per genotype). n.s., no significance, two-tailed unpaired Student's *t* test. ***B***, Quantification of BrdU$^+$ Nestin$^+$ and BrdU$^+$TBR2$^+$ cells in the SGZ region from adult control and *Chd8* iKO mice 3 h after BrdU administration. Data are means ± SEM ($n = 6$ animals per genotype). n.s., no significance, two-tailed unpaired Student's *t* test. ***C***. Left, Coronal sections of adult control and *Chd8* iKO SVZ regions immunostained for C-Casp3. Scale bars: 200 µm. DAPI, nuclei counterstain (blue). Right, Quantification of C-Casp3$^+$ cells. Data are means ± SEM ($n = 6$ animals per genotype); n.s., no significance, two-tailed unpaired Student's *t* test. ***D***, Left, Coronal sections of adult control and *Chd8* iKO SVZ regions immunostained for p53. Scale bars: 200 µm. DAPI, nuclei counterstain (blue). Right, Quantification of p53$^+$ cells. Data are means ± SEM ($n = 6$ animals per genotype); n.s., no significance, two-tailed unpaired Student's *t* test. ***E***, ***F***, Coronal sections of olfactory bulbs from adult control and *Chd8* iKO mice injected with TAM and immunostained for BrdU, NEUN, and CB (***E***) or TH (***F***). White arrows indicate triple-positive cells, which are newborn neurons. Scale bars: 50 µm. ***G***, ***H***, Quantification of percentage of BrdU$^+$/CB$^+$ (***G***) or BrdU$^+$/TH$^+$ (***H***) cells in olfactory bulbs of adult control and *Chd8* iKO mice. Data are means ± SEM ($n = 6$ animals/genotype); *$p < 0.05$; two-tailed unpaired Student's *t* test.

with controls (Fig. 10*E–H*). These data indicate that *Chd8* ablation results in a defect in interneuron differentiation during adult neurogenesis.

CHD8 loss-induced adult hippocampal neurogenesis defects ameliorated by proneurogenic fluoxetine treatment

As adult neurogenesis also occurs in the hippocampal SGZ, to investigate the effect of *Chd8* deletion on adult hippocampal neurogenesis, we induced *Chd8* deletion by administrating 8-week-old mice with tamoxifen. Four weeks after tamoxifen treatment, we labeled NSCs in the SGZ with BrdU injections for 5 d and harvested the brains of control and *Chd8* iKO mice at 2 d postinjection for assessing SGZ progenitor cell proliferation and 6 weeks postinjection for analyzing newly formed neurons, respectively (Battiste et al., 2007; Lagace et al., 2007; Fig. 11*A*). The number of BrdU$^+$ proliferative cells in the SGZ was comparable between control and *Chd8* iKO 2 d post-BrdU injection (Fig. 11*B*). However, at 6 weeks postinjection, the number of NeuN$^+$ newly formed mature neurons labeled with BrdU was reduced in *Chd8* iKO mice compared with controls (Fig. 11*C*), suggesting that *Chd8* ablation impairs neurogenesis in the SGZ region. As in the olfactory bulb region, we also observed a decrease in the number of DCX$^+$ newborn neurons in the SGZ (Fig. 11*D*,*E*). Similar to the SVZ region, we did not detect any significant alteration in NSC proliferation (marked by Ki67) in the SGZ region between control and *Chd8* iKO mice (Fig. 11*F*). These results suggest that the observed deficits in adult neurogenesis was not because of a decrease in the proliferation of NSCs in the SGZ as in the SVZ.

Given the defect in adult neurogenesis from NSCs in the absence of CHD8, we then tested whether a neurogenesis-promoting agent, the FDA-approved antidepressant FLX, could enhance NSC differentiation in *Chd8* iKO mice. Fluoxetine has been shown to promote adult neurogenesis and signaling pathways including WNT signaling (Santarelli et al., 2003; Ohira et al., 2013), which is a principal regulator of adult hippocampal neurogenesis (Lie et al., 2005) and downregulated in *Chd8* cKO cortices (Fig. 8). We then treated *Chd8* iKO and control mice with fluoxetine for 21 d and performed BrdU labeling to trace neurogenesis in the hippocampus (Fig. 11*G*). As expected, fluoxetine treatment increased neurogenesis in control mice (Fig. 11*H*). Strikingly, fluoxetine treatment increased BrdU-labeled newborn neurons in *Chd8* iKO adult mice compared with vehicle treatment (Fig. 11*I*,*J*). Moreover, DCX$^+$ neuroblasts also increased following fluoxetine treatment of *Chd8* iKO mice (Fig. 11*J*,*K*), despite at a lower number compared with that of control fluoxetine-treated group. These results indicate that fluoxetine treatment partially rescues the deficits in neurogenesis caused by loss of CHD8 in NSCs of adult mice, suggesting that enhancing NSC differentiation by fluoxetine, at least in part, restores the adult hippocampal neurogenesis defect in *Chd8* iKO mice.

Discussion

In this study, we use developmentally regulated ablation approaches to resolve CHD8 functions at different stages of neurogenesis. Our data demonstrate that CHD8 is not only required for NSC proliferation, survival, and proper cell cycle exit in the VZ but also, strikingly, for IPC production and survival in the SVZ at a critical period when IPC progenitors emerge in the embryonic

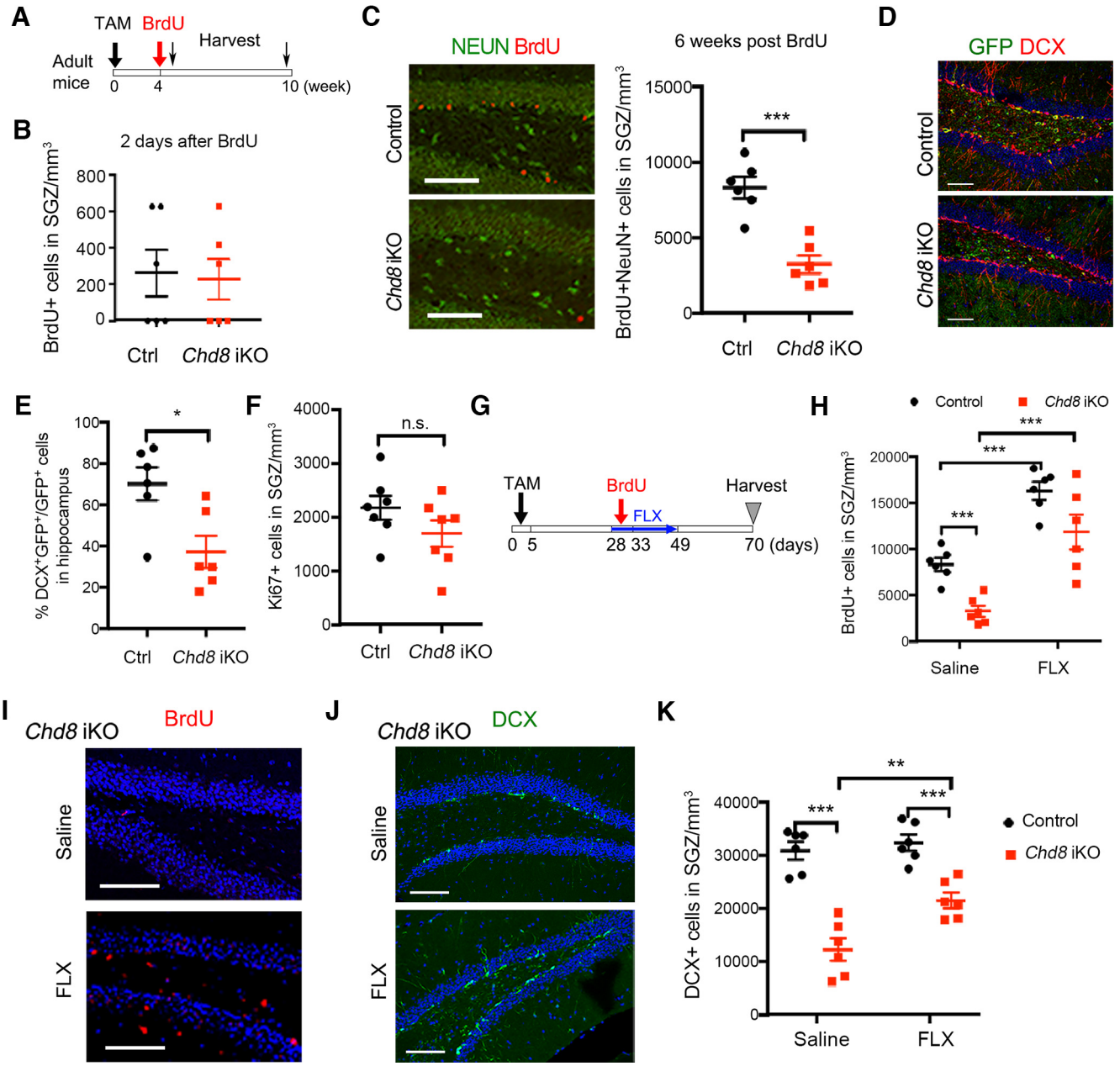

Figure 11. CHD8-loss-induced adult hippocampal neurogenesis defects rescued by fluoxetine treatment. ***A***, Schematic diagram of experimental design of TAM treatment and BrdU injection. ***B***, Quantification of $BrdU^+/NEUN^+$ cell numbers in SGZ from adult control and *Chd8* iKO mice harvested 2 d after BrdU injection. Data are means ± SEM ($n = 6$ animals per genotype). ***C***, Left, Coronal sections of SGZ from adult control and *Chd8* iKO mice harvested 6 weeks after BrdU injection and immunostained for BrdU and NEUN. Scale bars: 100 μm. Right, Quantification of $BrdU^+/NEUN^+$ cell numbers in SGZ from adult control and *Chd8* iKO mice harvested 6 weeks after BrdU injection. Data are means ± SEM ($n = 6$ animals per genotype); $^{***}p < 0.001$; two-tailed unpaired Student's *t* test. ***D***, Coronal sections of SGZ from adult control and *Chd8* iKO mice harvested 6 weeks after BrdU injection immunostained for DCX and GFP. Scale bars: 200 μm. DAPI, nuclei counterstain (blue). ***E***, Quantification of percentage of DCX^+GFP^+ cells in GFP^+ cells from adult control and *Chd8* iKO mice harvested 6 weeks after BrdU injection. Data are means ± SEM ($n = 6$ animals per genotype); $^*p < 0.05$; two-tailed unpaired Student's *t* test. ***F***, Quantification of $Ki67^+$ cells in the SGZ region from adult control and *Chd8* iKO mice at 6 weeks postinjection. Data are means ± SEM ($n = 7$ animals per genotype); n.s., no significance, two-tailed unpaired Student's *t* test. ***G***, Schematic diagram of experimental design of TAM administration, FLX treatment, and BrdU injection. ***H***, Quantification of $BrdU^+$ cell numbers in SGZ from control and *Chd8* iKO mice injected with TAM, BrdU, and treated with FLX. Data are means ± SEM ($n = 6$ animals per genotype); $^{***}p < 0.01$, two-tailed unpaired Student's *t* test. ***I***, ***J***, Coronal sections of SGZ from *Chd8* iKO mice injected with TAM, BrdU, and treated with saline or FLX then immunostained for BrdU (***I***) and DCX (***J***). Scale bars: ***I***, 100 μm; ***J***, 200 μm. DAPI, nuclei counterstain. ***K***, Quantification of DCX^+ cell numbers in the SGZ of *Chd8* iKO mice injected with TAM, BrdU, and treated with saline or FLX. Data are means ± SEM ($n = 6$ animals per genotype); $^{**}p < 0.01$, $^{***}p < 0.001$; two-tailed unpaired Student's *t* test.

cortex. The temporally specific analyses indicate that CHD8 is crucial for the transition from direct neurogenesis in the VZ to indirect neurogenesis in the SVZ. Thus, our studies identify a critical role of CHD8 for IPC-mediated indirect neurogenesis through controlling IPC production, survival, and differentiation into upper-layer neurons, in addition to direct neurogenesis at the early embryonic stages (Fig. 8). Given that the upper-layer excitatory cortical neurons are preferentially impaired in autistic brains (Velmeshev et al., 2019), the discovery of an important role of CHD8 in IPC generation and upper-layer neuron production is relevant to human ASD phenotypes.

Consistent with CHD8 inhibition of p53 transactivation (Nishiyama et al., 2009), we detect massive apoptosis for PAX6-positive NPCs in the VZ along with upregulation of

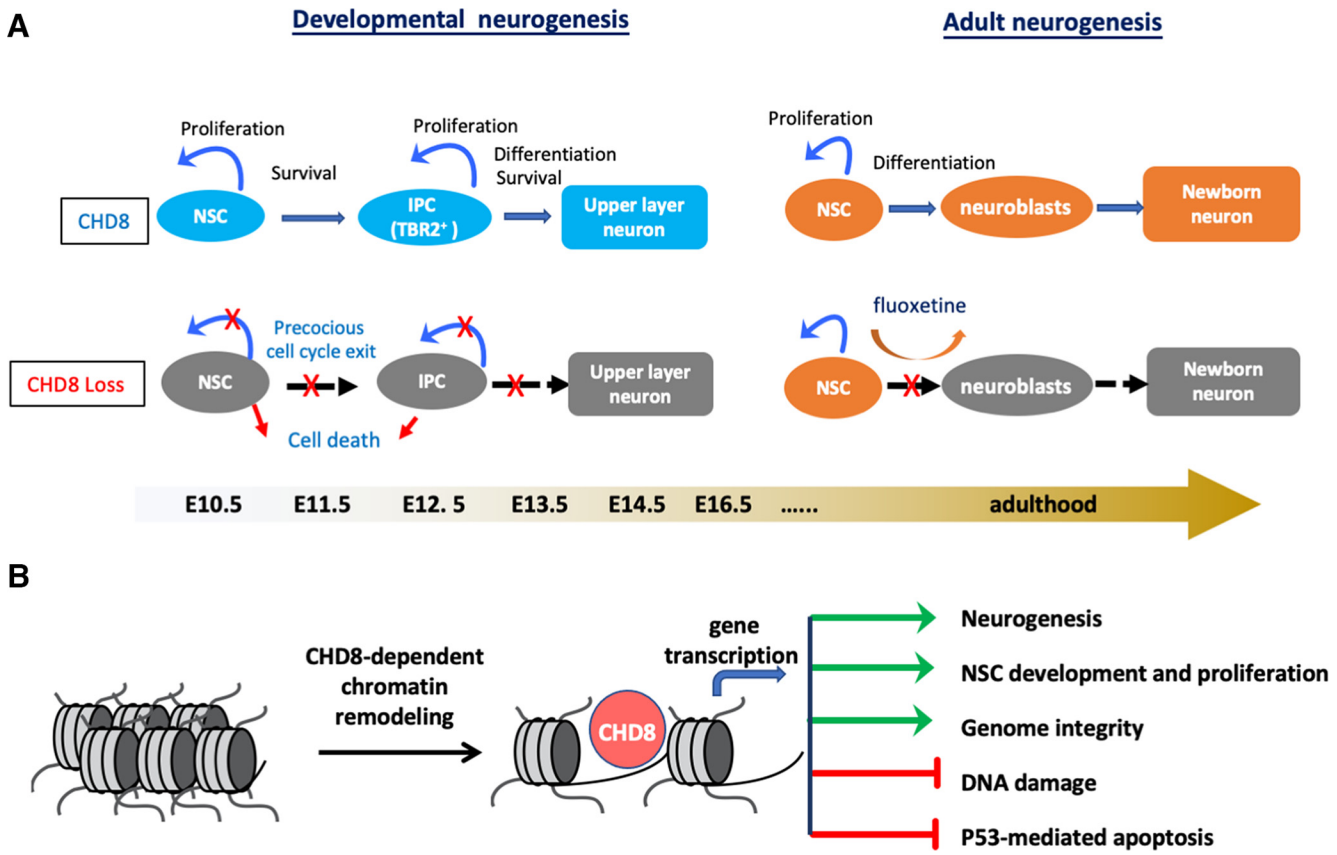

Figure 12. Stage-specific CHD8 functions in developmental and adult neurogenesis. ***A***, Schematic diagram shows that CHD8 is required for direct and indirect neurogenesis as well as adult neurogenesis through distinct effects. In the developing cortex, CHD8 ablation in the embryonic cortical progenitor cells disrupts multiple developmental processes including NPC proliferation and survival and $TBR2^+$ IPC differentiation and survival, as well as leads to precocious cell cycle exit. Temporally specific CHD8 ablation reveals that the loss of the IPC population contributes to the defects in the production of upper-layer neurons. In the adult brain, unlike in the embryonic brain, CHD8 loss does not affect adult NSC proliferation and survival but impairs adult neurogenesis by disrupting DCX^+ or $TBR2^+$ IPC-associated neuroblasts for newborn neuron differentiation from adult NSCs. Fluoxetine treatment can partially restore adult neurogenesis defects in the *Chd8* mutants. ***B***, Schematic diagram shows that CHD8 can directly target and regulate the chromatin landscape of key regulatory genes associated with NSC proliferation and stemness as well as neuronal differentiation while maintaining genomic integrity against DNA-damage-induced apoptotic cell death.

DNA damage marker γH2A.X and p53 in *Chd8* cKO cortices at early embryonic stages but to a less extent for $TUJ1^+$ neurons. This is in contrast to the predominantly $TUJ1^+$ apoptotic cells reported in *Emx1-Cre;Chd8*$^{fl/fl\text{-}Exon3}$ mice (Kweon et al., 2021). This phenotypic discrepancy might be because of the nature of the mutations disrupting specific *Chd8* isoforms (exon-4 vs exon-3; Kunkel et al., 2018; Lee et al., 2020). Importantly, we find that *Chd8* ablation causes NPC death at the early embryonic stages (e.g., E11.5), but not at the late embryonic stages after E13.5. In adults, *Chd8*-inducible ablation in NSCs also does not lead to apoptosis. Thus, our data indicate that CHD8 regulates p53 expression and NPC survival in a stage-dependent manner, suggesting that CHD8 does not function as a general inhibitor of p53 transactivation and apoptosis as previously proposed (Nishiyama et al., 2009) but rather maintains genomic integrity and protects against apoptosis on DNA damage at the early embryonic stages, which is particularly detrimental to the rapidly dividing neural progenitors (Allard et al., 2004; Sokpor et al., 2018).

In the hippocampus of *Chd8* cKO mice, CA3 and CA1 regions appear to be completely disrupted; the dentate gyrus can be detected, however, its size is much smaller compared with controls, implicating an impairment of adult neurogenesis. CHD8 depletion does not impair the proliferation and survival of adult NSCs, unlike those defects observed in the early embryonic cortex of *Chd8* mutants, yet it impedes the differentiation of DCX^+ newborn neurons from adult NSCs, leading to the decline in adult neurogenesis (Fig. 12). The stark contrast between early embryonic neurogenesis and later embryonic and adult neurogenesis might be because of the intrinsic differences in embryonic and adult neural progenitors, and extrinsic differences of NSC niches, or both. Similar phenotypes have been reported for another CHD family member, CHD7, which is required for embryonic neural differentiation but dispensable for NSC self-renewal during adult neurogenesis (Feng et al., 2013). CHD7 or other family members might compensate for CHD8 loss at the later stages, as CHD7 and CHD8 can work together to regulate NSC survival and differentiation (Feng et al., 2013; Marie et al., 2018). Nonetheless, the defect in IPC and newborn neuron production in the *Chd8*-ablated adult brain suggests a previously unrecognized critical role of CHD8 for adult neurogenesis and neuronal lineage transition from adult NSC niches.

Although macrocephaly has been associated with CHD8 mutations in patients and systemic haploinsufficiency in *Chd8* heterozygous (*Chd8*$^{+/-}$) mutant mice (Katayama et al., 2016; Gompers et al., 2017; Suetterlin et al., 2018; Sood et al., 2020; Hurley et al., 2021), we did not observe a macrocephaly phenotype in the NSC-specific *Chd8* cHet and cKO mice, consistent with another *Emx1-Cre;Chd8* mutant mice (Kweon et al., 2021). These differences may result because of neural-progenitor-specific versus systemic CHD8 haploinsufficiency. In our NSC-specific *Chd8* cHet animals, *Chd8* dose is reduced predominantly in

the neural progenitors of the cortex, whereas in *Chd8* heterozygous or hypomorph animals, CHD8 dose decreases systematically in all brain cells, which may lead to changes in neuropil compositions. In addition, the phenotypic variation between the haploinsufficient human *CHD8* mutants and NSC-specific *Chd8* cHet mice might be because of a differential sensitivity to gene dosage across species, genetic backgrounds, or both. It is worth noting that patient phenotypes with CHD8 mutations are heterogeneous (Bernier et al., 2014; An and Claudianos, 2016; Courchesne et al., 2019). A cohort of patients with disruptive CHD8 mutations exhibited developmental defects or delay (Bernier et al., 2014; Zhao et al., 2018), which might be potentially related to the phenotype observed in the mice with homozygous CHD8 loss in NPCs.

Initial studies used constitutive *Chd8* heterozygous mice or knockdown models to examine the functions of CHD8 in ASD-related phenotypes (Durak et al., 2016; Katayama et al., 2016; Gompers et al., 2017; Platt et al., 2017; Jung et al., 2018). However, the findings from these earlier studies were complicated by stage- and dosage-dependent roles for CHD8 in neural development (Sood et al., 2020; Hurley et al., 2021). Our NPC cell-type- and stage-specific *in vivo* mutagenesis analyses delineate a conserved and distinct role of CHD8 for direct and indirect neurogenesis at early embryonic stages and adult neurogenesis. Although cortical developmental defects in *Chd8* cKO animals are consistent with previous reported *Emx1-Cre;* $Chd8^{fl/fl\text{-}Exon\text{-}3}$ and *Sox1-Cre*;$Chd8^{fl/f}$ mice (Hurley et al., 2021; Kweon et al., 2021), we detected phenotypic and behavior differences between our and previously reported *Chd8*-mutant mice. In heterozygous *Chd8* cHet littermates, we did not observe any significant alteration of NSC proliferation and survival, which is in contrast with a reported increase in proliferative NSCs and SVZ progenitors in the $Chd8^{+/-}$ embryonic cortex (Gompers et al., 2017). Moreover, in contrast to an increase in $TBR2^+$ IPCs as reported in hypomorph $Chd8^{neo/neo}$ embryos (Hurley et al., 2021), we observed a decrease in $TBR2^+$ IPCs and an increase on IPC cell death in NPC-specific *Chd8* cKO animals. In addition, our *Chd8* cKO mice exhibit increased anxiety-like behavior and decreased socialization, characteristics of ASD (Frye, 2018; Hollocks et al., 2019). This is in contrast to the previous report for the decreased anxiety and increased preference of social novelty in *Emx1-Cre*;$Chd8^{fl/fl\text{-}Exon\text{-}3}$ mice (Kweon et al., 2021). This might be because of differences in *Chd8* mutations (e.g., exon-4 vs exon-3 deletion), as suggested by the alternative splicing forms of *Chd8* (Kunkel et al., 2018; Lee et al., 2020), the extent of defects in neural cell-type formation, or even different experimental conditions. Nonetheless, our behavioral results are consistent with another hypomorph model that reduced CHD8 levels below those of heterozygotes (Hurley et al., 2021). Future work will be required to directly compare these different *Chd8* mutant models to determine the specific impact of CHD8 loss on cortical cell-type development and animal behaviors.

Transcriptomics analysis revealed that the genes associated with neurogenesis and neural differentiation were downregulated in *Chd8* cKO mice, similar to those from systemic heterozygous $Chd8^{+/-}$ mice (Katayama et al., 2016; Gompers et al., 2017; Platt et al., 2017; Suetterlin et al., 2018) and hypomorph $Chd8^{neo/neo}$ mice (Hurley et al., 2021). However, functional requirements of CHD8 in NPC development are in stark contrast to those during neural differentiation from ESCs, wherein CHD8 inhibits neuronal gene expression and maintains pluripotency (Sood et al., 2020). CHD8 might play a distinct role in specification from ESCs to NPCs versus differentiation from NPCs to neurons. WNT signaling was downregulated in *Chd8* cKO mice, consistent with findings from *in utero* knockdown (Durak et al., 2016); however, it was upregulated in the brain of some *Chd8*-heterozygous mice at E14.5 (Katayama et al., 2016; Platt et al., 2017). The discrepancy in transcriptomics data across different *Chd8* mutants might be because of the differences in cell types, brain regions, and dosage with *Chd8* deficiency. Nonetheless, our integrated genomic and transcriptomic analyses reveal that CHD8 can directly target and regulate the chromatin landscape of key regulatory genes associated with NSC development and neuronal differentiation and provide a functional link between the chromatin accessibility landscape and cell-survival- and neurogenesis-promoting programs regulated by CHD8 in neural progenitors.

The FDA-approved antidepressant fluoxetine has been shown to stimulate adult neurogenesis (Santarelli et al., 2003; Kong et al., 2009; Ohira et al., 2013) and attenuates autistic behaviors including obsessive-compulsive behaviors in ASD (Reddihough et al., 2019). We showed that fluoxetine treatment can at least partially overcome adult neurogenesis deficits because of CHD8 loss. Fluoxetine has been shown to regulate multiple signaling pathways including WNT, serotonin, and glucocorticoid signaling for neurogenesis (Santarelli et al., 2003; Ohira et al., 2013; Lee et al., 2016; Cunha et al., 2018), although the exact mechanisms underlying adult neurogenesis remain to be further defined.

References

Aimone JB, Wiles J, Gage FH (2006) Potential role for adult neurogenesis in the encoding of time in new memories. Nat Neurosci 9:723–727.

Allard S, Masson JY, Côté J (2004) Chromatin remodeling and the maintenance of genome integrity. Biochim Biophys Acta 1677:158–164.

An JY, Claudianos C (2016) Genetic heterogeneity in autism: from single gene to a pathway perspective. Neurosci Biobehav Rev 68:442–453.

Battiste J, Helms AW, Kim EJ, Savage TK, Lagace DC, Mandyam CD, Eisch AJ, Miyoshi G, Johnson JE (2007) Ascl1 defines sequentially generated lineage-restricted neuronal and oligodendrocyte precursor cells in the spinal cord. Development 134:285–293.

Bernier R, et al. (2014) Disruptive CHD8 mutations define a subtype of autism early in development. Cell 158:263–276.

Borrell V (2019) Recent advances in understanding neocortical development. F1000Res 8:1791.

Buenrostro JD, Wu B, Chang HY, Greenleaf WJ (2015) ATAC-seq: a method for assaying chromatin accessibility genome-wide. Curr Protoc Mol Biol 109:21.29.1–21.29.9.

Cardenas A, Villalba A, de Juan Romero C, Pico E, Kyrousi C, Tzika AC, Tessier-Lavigne M, Ma L, Drukker M, Cappello S, Borrell V (2018) Evolution of cortical neurogenesis in amniotes controlled by robo signaling levels. Cell 174:590–606.e21.

Cotney J, Muhle RA, Sanders SJ, Liu L, Willsey AJ, Niu W, Liu W, Klei L, Lei J, Yin J, Reilly SK, Tebbenkamp AT, Bichsel C, Pletikos M, Sestan N, Roeder K, State MW, Devlin B, Noonan JP (2015) The autism-associated chromatin modifier CHD8 regulates other autism risk genes during human neurodevelopment. Nat Commun 6:6404.

Courchesne E, Pramparo T, Gazestani VH, Lombardo MV, Pierce K, Lewis NE (2019) The ASD living biology: from cell proliferation to clinical phenotype. Mol Psychiatry 24:88–107.

Cunha V, Rodrigues P, Santos MM, Moradas-Ferreira P, Ferreira M (2018) Fluoxetine modulates the transcription of genes involved in serotonin, dopamine and adrenergic signalling in zebrafish embryos. Chemosphere 191:954–961.

Delgado RN, Mansky B, Ahanger SH, Lu C, Andersen RE, Dou Y, Alvarez-Buylla A, Lim DA (2020) Maintenance of neural stem cell positional identity by mixed-lineage leukemia 1. Science 368:48–53.

Deng W, Aimone JB, Gage FH (2010) New neurons and new memories: how does adult hippocampal neurogenesis affect learning and memory? Nat Rev Neurosci 11:339–350.

Durak O, Gao F, Kaeser-Woo YJ, Rueda R, Martorell AJ, Nott A, Liu CY, Watson LA, Tsai LH (2016) Chd8 mediates cortical neurogenesis via transcriptional regulation of cell cycle and Wnt signaling. Nat Neurosci 19:1477–1488.

Ellingford RA, Panasiuk MJ, de Meritens ER, Shaunak R, Naybour L, Browne L, Basson MA, Andreae LC (2021) Cell-type-specific synaptic imbalance and disrupted homeostatic plasticity in cortical circuits of ASD-associated Chd8 haploinsufficient mice. Mol Psychiatry 26:3614–3624.

Feng W, Khan MA, Bellvis P, Zhu Z, Bernhardt O, Herold-Mende C, Liu HK (2013) The chromatin remodeler CHD7 regulates adult neurogenesis via activation of SoxC transcription factors. Cell Stem Cell 13:62–72.

Florio M, Huttner WB (2014) Neural progenitors, neurogenesis and the evolution of the neocortex. Development 141:2182–2194.

Frye RE (2018) Social skills deficits in autism spectrum disorder: potential biological origins and progress in developing therapeutic agents. CNS Drugs 32:713–734.

Gompers AL, et al. (2017) Germline Chd8 haploinsufficiency alters brain development in mouse. Nat Neurosci 20:1062–1073.

Gorski JA, Talley T, Qiu M, Puelles L, Rubenstein JL, Jones KR (2002) Cortical excitatory neurons and glia, but not GABAergic neurons, are produced in the Emx1-expressing lineage. J Neurosci 22:6309–6314.

Gould TD, Dao DT, Kovacsics CE (2009) The open field test. In: Mood and anxiety related phenotypes in mice: characterization using behavioral tests. (Gould TD, ed), pp 1–20. Totowa, New Jersey: Humana.

Hollocks MJ, Lerh JW, Magiati I, Meiser-Stedman R, Brugha TS (2019) Anxiety and depression in adults with autism spectrum disorder: a systematic review and meta-analysis. Psychol Med 49:559–572.

Hsieh J, Gage FH (2004) Epigenetic control of neural stem cell fate. Curr Opin Genet Dev 14:461–469.

Hsieh J, Zhao X (2016) Genetics and epigenetics in adult neurogenesis. Cold Spring Harb Perspect Biol 8:a018911.

Hurley S, Mohan C, Suetterlin P, Ellingford R, Riegman KLH, Ellegood J, Caruso A, Michetti C, Brock O, Evans R, Rudari F, Delogu A, Scattoni ML, Lerch JP, Fernandes C, Basson MA (2021) Distinct, dosage-sensitive requirements for the autism-associated factor CHD8 during cortical development. Mol Autism 12:16.

Imayoshi I, Ohtsuka T, Metzger D, Chambon P, Kageyama R (2006) Temporal regulation of Cre recombinase activity in neural stem cells. Genesis 44:233–238.

Insolera R, Bazzi H, Shao W, Anderson KV, Shi SH (2014) Cortical neurogenesis in the absence of centrioles. Nat Neurosci 17:1528–1535.

Jiménez JA, Ptacek TS, Tuttle AH, Schmid RS, Moy SS, Simon JM, Zylka MJ (2020) Chd8 haploinsufficiency impairs early brain development and protein homeostasis later in life. Mol Autism 11:74.

Jung H, et al. (2018) Sexually dimorphic behavior, neuronal activity, and gene expression in Chd8-mutant mice. Nat Neurosci 21:1218–1228.

Kaidanovich-Beilin O, Lipina T, Vukobradovic I, Roder J, Woodgett JR (2011) Assessment of social interaction behaviors. J Vis Exp 2011:2473.

Katayama Y, Nishiyama M, Shoji H, Ohkawa Y, Kawamura A, Sato T, Suyama M, Takumi T, Miyakawa T, Nakayama KI (2016) CHD8 haploinsufficiency results in autistic-like phenotypes in mice. Nature 537:675–679.

Kong H, Sha LL, Fan Y, Xiao M, Ding JH, Wu J, Hu G (2009) Requirement of AQP4 for antidepressive efficiency of fluoxetine: implication in adult hippocampal neurogenesis. Neuropsychopharmacology 34:1263–1276.

Kraeuter AK, Guest PC, Sarnyai Z (2019) The open field test for measuring locomotor activity and anxiety-like behavior. Methods Mol Biol 1916:99–103.

Kriegstein A, Alvarez-Buylla A (2009) The glial nature of embryonic and adult neural stem cells. Annu Rev Neurosci 32:149–184.

Kunkel GR, Tracy JA, Jalufka FL, Lekven AC (2018) CHD8short, a naturally-occurring truncated form of a chromatin remodeler lacking the helicase domain, is a potent transcriptional coregulator. Gene 641:303–309.

Kweon H, et al. (2021) Excitatory neuronal CHD8 in the regulation of neocortical development and sensory-motor behaviors. Cell Rep 34:108780.

Lagace DC, Whitman MC, Noonan MA, Ables JL, DeCarolis NA, Arguello AA, Donovan MH, Fischer SJ, Farnbauch LA, Beech RD, DiLeone RJ, Greer CA, Mandyam CD, Eisch AJ (2007) Dynamic contribution of nestin-expressing stem cells to adult neurogenesis. J Neurosci 27:12623–12629.

Lee CY, Petkova M, Morales-Gonzalez S, Gimber N, Schmoranzer J, Meisel A, Böhmerle W, Stenzel W, Schuelke M, Schwarz JM (2020) A spontaneous missense mutation in the chromodomain helicase DNA-binding protein 8 (CHD8) gene: a novel association with congenital myasthenic syndrome. Neuropathol Appl Neurobiol 46:588–601.

Lee MS, Kim YH, Park WS, Park OK, Kwon SH, Hong KS, Rhim H, Shim I, Morita K, Wong DL, Patel PD, Lyons DM, Schatzberg AF, Her S (2016) Temporal variability of glucocorticoid receptor activity is functionally important for the therapeutic action of fluoxetine in the hippocampus. Mol Psychiatry 21:252–260.

Lie DC, Colamarino SA, Song HJ, Désiré L, Mira H, Consiglio A, Lein ES, Jessberger S, Lansford H, Dearie AR, Gage FH (2005) Wnt signalling regulates adult hippocampal neurogenesis. Nature 437:1370–1375.

Liu W, Zhou H, Liu L, Zhao C, Deng Y, Chen L, Wu L, Mandrycky N, McNabb CT, Peng Y, Fuchs PN, Lu J, Sheen V, Qiu M, Mao M, Lu QR (2015) Disruption of neurogenesis and cortical development in transgenic mice misexpressing Olig2, a gene in the Down syndrome critical region. Neurobiol Dis 77:106–116.

Lord C, Elsabbagh M, Baird G, Veenstra-Vanderweele J (2018) Autism spectrum disorder. Lancet 392:508–520.

Lu F, et al. (2016) Olig2-dependent reciprocal shift in PDGF and EGF receptor signaling regulates tumor phenotype and mitotic growth in malignant glioma. Cancer Cell 29:669–683.

Lui JH, Hansen DV, Kriegstein AR (2011) Development and evolution of the human neocortex. Cell 146:18–36.

Marie C, Clavairoly A, Frah M, Hmidan H, Yan J, Zhao C, Van Steenwinckel J, Daveau R, Zalc B, Hassan B, Thomas JL, Gressens P, Ravassard P, Moszer I, Martin DM, Lu QR, Parras C (2018) Oligodendrocyte precursor survival and differentiation requires chromatin remodeling by Chd7 and Chd8. Proc Natl Acad Sci U S A 115:E8246–E8255.

Merkle FT, Mirzadeh Z, Alvarez-Buylla A (2007) Mosaic organization of neural stem cells in the adult brain. Science 317:381–384.

Mihalas AB, Elsen GE, Bedogni F, Daza RAM, Ramos-Laguna KA, Arnold SJ, Hevner RF (2016) Intermediate progenitor cohorts differentially generate cortical layers and require Tbr2 for timely acquisition of neuronal subtype identity. Cell Rep 16:92–105.

Ming GL, Song H (2011) Adult neurogenesis in the mammalian brain: significant answers and significant questions. Neuron 70:687–702.

Molyneaux BJ, Arlotta P, Menezes JR, Macklis JD (2007) Neuronal subtype specification in the cerebral cortex. Nat Rev Neurosci 8:427–437.

Nishiyama M, Oshikawa K, Tsukada Y, Nakagawa T, Iemura S, Natsume T, Fan Y, Kikuchi A, Skoultchi AI, Nakayama KI (2009) CHD8 suppresses p53-mediated apoptosis through histone H1 recruitment during early embryogenesis. Nat Cell Biol 11:172–182.

Noctor SC, Martínez-Cerdeño V, Ivic L, Kriegstein AR (2004) Cortical neurons arise in symmetric and asymmetric division zones and migrate through specific phases. Nat Neurosci 7:136–144.

Obernier K, Cebrian-Silla A, Thomson M, Parraguez JI, Anderson R, Guinto C, Rodas Rodriguez J, Garcia-Verdugo JM, Alvarez-Buylla A (2018) Adult neurogenesis is sustained by symmetric self-renewal and differentiation. Cell Stem Cell 22:221–234.e8.

Ohira K, Takeuchi R, Shoji H, Miyakawa T (2013) Fluoxetine-induced cortical adult neurogenesis. Neuropsychopharmacology 38:909–920.

Packer A (2016) Neocortical neurogenesis and the etiology of autism spectrum disorder. Neurosci Biobehav Rev 64:185–195.

Platt RJ, Zhou Y, Slaymaker IM, Shetty AS, Weisbach NR, Kim JA, Sharma J, Desai M, Sood S, Kempton HR, Crabtree GR, Feng G, Zhang F (2017) Chd8 mutation leads to autistic-like behaviors and impaired striatal circuits. Cell Rep 19:335–350.

Reddihough DS, Marraffa C, Mouti A, O'Sullivan M, Lee KJ, Orsini F, Hazell P, Granich J, Whitehouse AJO, Wray J, Dossetor D, Santosh P, Silove N, Kohn M (2019) Effect of fluoxetine on obsessive-compulsive behaviors in children and adolescents with autism spectrum disorders: a randomized clinical trial. JAMA 322:1561–1569.

Santarelli L, Saxe M, Gross C, Surget A, Battaglia F, Dulawa S, Weisstaub N, Lee J, Duman R, Arancio O, Belzung C, Hen R (2003) Requirement of hippocampal neurogenesis for the behavioral effects of antidepressants. Science 301:805–809.

Seibenhener ML, Wooten MC (2015) Use of the Open Field Maze to measure locomotor and anxiety-like behavior in mice. J Vis Exp 2015:e52434.

Sessa A, Mao CA, Hadjantonakis AK, Klein WH, Broccoli V (2008) Tbr2 directs conversion of radial glia into basal precursors and guides neuronal amplification by indirect neurogenesis in the developing neocortex. Neuron 60:56–69.

Simonoff E, Pickles A, Charman T, Chandler S, Loucas T, Baird G (2008) Psychiatric disorders in children with autism spectrum disorders: prevalence, comorbidity, and associated factors in a population-derived sample. J Am Acad Child Adolesc Psychiatry 47:921–929.

Sokpor G, Castro-Hernandez R, Rosenbusch J, Staiger JF, Tuoc T (2018) ATP-dependent chromatin remodeling during cortical neurogenesis. Front Neurosci 12:226.

Song J, Christian KM, Ming GL, Song H (2012) Modification of hippocampal circuitry by adult neurogenesis. Dev Neurobiol 72:1032–1043.

Sood S, Weber CM, Hodges HC, Krokhotin A, Shalizi A, Crabtree GR (2020) CHD8 dosage regulates transcription in pluripotency and early murine neural differentiation. Proc Natl Acad Sci U S A 117:22331–22340.

Stolerman ES, Smith B, Chaubey A, Jones JR (2016) CHD8 intragenic deletion associated with autism spectrum disorder. Eur J Med Genet 59:189–194.

Suetterlin P, Hurley S, Mohan C, Riegman KLH, Pagani M, Caruso A, Ellegood J, Galbusera A, Crespo-Enriquez I, Michetti C, Yee Y, Ellingford R, Brock O, Delogu A, Francis-West P, Lerch JP, Scattoni ML, Gozzi A, Fernandes C, Basson MA (2018) Altered neocortical gene expression, brain overgrowth and functional over-connectivity in Chd8 haploinsufficient mice. Cereb Cortex 28:2192–2206.

Takumi T, Tamada K, Hatanaka F, Nakai N, Bolton PF (2020) Behavioral neuroscience of autism. Neurosci Biobehav Rev 110:60–76.

Varghese M, Keshav N, Jacot-Descombes S, Warda T, Wicinski B, Dickstein DL, Harony-Nicolas H, De Rubeis S, Drapeau E, Buxbaum JD, Hof PR (2017) Autism spectrum disorder: neuropathology and animal models. Acta Neuropathol 134:537–566.

Vasistha NA, García-Moreno F, Arora S, Cheung AF, Arnold SJ, Robertson EJ, Molnár Z (2015) Cortical and clonal contribution of Tbr2 expressing progenitors in the developing mouse brain. Cereb Cortex 25:3290–3302.

Velmeshev D, Schirmer L, Jung D, Haeussler M, Perez Y, Mayer S, Bhaduri A, Goyal N, Rowitch DH, Kriegstein AR (2019) Single-cell genomics identifies cell type-specific molecular changes in autism. Science 364:685–689.

Williams AB, Schumacher B (2016) p53 in the DNA-damage-repair process. Cold Spring Harb Perspect Med 6:a026070.

Xu Q, Liu YY, Wang X, Tan GH, Li HP, Hulbert SW, Li CY, Hu CC, Xiong ZQ, Xu X, Jiang YH (2018) Autism-associated CHD8 deficiency impairs axon development and migration of cortical neurons. Mol Autism 9:65.

Zhao C, Dong C, Frah M, Deng Y, Marie C, Zhang F, Xu L, Ma Z, Dong X, Lin Y, Koenig S, Nait-Oumesmar B, Martin DM, Wu LN, Xin M, Zhou W, Parras C, Lu QR (2018) Dual requirement of CHD8 for chromatin landscape establishment and histone methyltransferase recruitment to promote CNS myelination and repair. Dev Cell 45:753–768.e8.